

A Theoretically Guaranteed Quaternion Weighted Schatten p -norm Minimization Method for Color Image Restoration

Qinghua Zhang · Liangtian He · Yilun Wang · Liang-Jian Deng · Jun Liu

Received: date / Accepted: date

Abstract Inspired by the fact that the matrix formulated by nonlocal similar patches in a natural image is of low rank, the rank approximation issue have been extensively investigated over the past decades, among which weighted nuclear norm minimization (WNNM) and weighted Schatten p -norm minimization (WSNM) are two prevailing methods have shown great superiority in various image restoration (IR) problems. Due to the physical characteristic of color images, color image restoration (CIR) is often a much more difficult task than its grayscale image counterpart. However, when applied to CIR, the

Qinghua Zhang

Key Laboratory of Intelligent Computing and Signal Processing of Ministry of Education, School of Mathematical Sciences, Anhui University, Hefei 230601, People's Republic of China.

E-mail: qinghuaz@stu.ahu.edu.cn

Liangtian He

Key Laboratory of Intelligent Computing and Signal Processing of Ministry of Education, School of Mathematical Sciences, Anhui University, Hefei 230601, People's Republic of China.

E-mail: helt@ahu.edu.cn

Yilun Wang

Machinify Inc, Palo Alto, California 94301, United States.

E-mail: yilun.wang@gmail.com

Liang-Jian Deng

School of Mathematical Sciences, University of Electronic Science and Technology of China, Chengdu 611731, People's Republic of China.

E-mail: liangjian.deng@uestc.edu.cn

Jun Liu

Key Laboratory for Applied Statistics of MOE, School of Mathematics and Statistics, Northeast Normal University, Changchun 130024, People's Republic of China.

E-mail: liuj292@nenu.edu.cn

traditional WNNM/WSNM method only processes three color channels individually and fails to consider their cross-channel correlations. Very recently, a quaternion-based WNNM approach (QWNNM) has been developed to mitigate this issue, which is capable of representing the color image as a whole in the quaternion domain and preserving the inherent correlation among the three color channels. Despite its empirical success, unfortunately, the convergence behavior of QWNNM has not been strictly studied yet. In this paper, on the one side, we extend the WSNM into quaternion domain and correspondingly propose a novel quaternion-based WSNM model (QWSNM) for tackling the CIR problems. Extensive experiments on two representative CIR tasks, including color image denoising and deblurring, demonstrate that the proposed QWSNM method performs favorably against many state-of-the-art alternatives, in both quantitative and qualitative evaluations. On the other side, more importantly, we preliminarily provide a theoretical convergence analysis, that is, by modifying the quaternion alternating direction method of multipliers (QADMM) through a simple continuation strategy, we theoretically prove that both the solution sequences generated by the QWNNM and QWSNM have fixed-point convergence guarantees. The source code of our algorithm can be downloaded at the website: <https://github.com/qiuxuanzhizi/QWSNM>.

Keywords Weighted nuclear norm minimization · Weighted Schatten p -norm minimization · Color image restoration · Quaternion representation · Quaternion ADMM

1 Introduction

Due to the imperfections of imaging systems and inevitable interference of external factors, the acquired images are often degraded in the process of image acquisition, transmission, and storage. Restoring the clean high-quality image from the corrupted one has been a long-standing research topic for its highly practical value. It is often acted as a crucial preprocessing step for the success of subsequent various high-level applications, such as detection, classification, recognition, segmentation, and so on. Let an $m \times n$ image with q channels be lexicographically stacked by $\mathbf{x} = [\mathbf{x}^{(1)}, \mathbf{x}^{(2)}, \dots, \mathbf{x}^{(q)}] \in \mathbb{R}^{qmn}$, where $\mathbf{x}^{(i)} \in \mathbb{R}^{mn}$ represents the i -th channel for $i = 1, 2, \dots, q$. Mathemati-

cally, the degradation process is generally formulated as:

$$\mathbf{y} = \mathbf{A}\mathbf{x} + \mathbf{n}, \quad (1)$$

where $\mathbf{A} \in \mathbb{R}^{qmn \times qmn}$ is a linear degraded operator¹, typically a convolution operator in image deblurring and an identity matrix in image denoising, $\mathbf{x} \in \mathbb{R}^{qmn}$ and $\mathbf{y} \in \mathbb{R}^{qmn}$ are the underlying clean image and corrupted observation, respectively. \mathbf{n} is normally assumed to be the additive white Gaussian noise (AWGN) with variance σ^2 . Since a significant amount of information has been lost during the degradation process, image restoration (IR) is typically an ill-posed problem, making the recovery of clean image from its degraded one rather challenging. To compensate for the information loss, as a common used strategy, appropriate prior information of the interested image (also known as regularization) often needs to be introduced to alleviate the ill-posedness by constraining the solution space. During the last several decades, there have been enduring efforts to the prior exploration, such as total variation (TV) regularized methods [1–4], sparse representation methods [5–7], nonlocal self-similarity (NSS) prior methods [8, 9], low-rank regularized methods [10–12], denoiser-guided methods [13, 14], etc.

As an important branch, low rank matrix approximation (LRMA) has been widely applied in numerous IR tasks, which intents on recovering the underlying low rank matrix from its degraded observation. Generally, the LRMA can be divided into two categories: low rank matrix factorization (LRMF) methods [15–18] and low rank minimization (LRM) methods [19–21]. LRMF assumes the latent matrix is a product of two low-rank matrices. However, a significant shortcoming limiting its practical applicability is that the rank of underlying matrix often can not be easily predetermined. By contrast, LRM usually solves a minimization problem with different rank approximation regularizers, such as the widely used nuclear norm. Candès et al. [22] has proven that nuclear norm is the tightest convex relaxation of the NP-hard rank function. Despite a good theoretical guarantee by the singular value thresholding (SVT) operation, many studies have demonstrated that the nuclear norm minimization (NNM) tends to yield sub-optimal solutions of the original rank minimization. The main reason behind this phenomenon is that NNM treats each singular value

¹ In this paper, we mainly focus on the color image denoising and deblurring, note that the extension to other color image restoration tasks would be straightforward.

equally, which conflicts with the fact that the larger singular values often contain more information and should be penalized slightly. In order to enhance the stability and effectiveness of the nuclear norm regularization, many nonconvex surrogates have been introduced instead. Among them, one of the most representative work is the nonlocal patch-based weighted NNM model (WNNM) proposed by [23] for grayscale image denoising, which considers the physical significance of the singular values and assigns different weights to them. In subsequent research, Gu et al. [24] further extended WNNM to other low-level vision tasks, including background subtraction, color image denoising and inpainting. It is worth emphasizing that though WNNM often delivers promising results, it still tends to over-shrink the dominant rank components, which constrains its capacity of recovering the images with rich textures and details. To overcome this shortcoming, based on the Schatten p -norm minimization (SNM) [25], Xie et al. [26] proposed a more effective weighted Schatten p -norm minimization (WSNM) model, which avoids shrinking too much the low rank components and is capable of obtaining more accurate recovery results compared to the WNNM counterpart. Similarly, Zha et al. [27] proposed a non-convex weighted ℓ_p nuclear norm minimization (NCW-NNM) model under the ADMM framework for IR problems.

Given the rapidly growing role of color images in our daily life, the color image restoration (CIR) has received increasingly attention in this research field. It should be pointed out that most of the existing IR algorithms are originally developed for grayscale images (i.e., single channel). For more complicated CIR problems, the easiest and rudest way is to implement these IR approaches on three color channels (i.e., red, green, and blue in the RGB color space) individually. Unfortunately, this straightforward extension through a channel-wise manner commonly yields unsatisfactory results since they totally ignore the inter-channel correlation between RGB components. Alternatively, two other practicable strategies have been widely adopted to CIR [28]. The first strategy is to convert the color images from standard RGB space into a less correlated color space, such as YCbCr space, and then restore each color channel in the transformed space independently. For example, the color block-matching and 3D filtering (CBM3D) [29] first converts the sRGB image into a luminance-chrominance space and then applies BM3D to each channel separately. The second strategy is to concatenate the three RGB channels to make

use of the channel correlation. For instance, Xu et al. [30] proposed a multi-channel WNNM (MC-WNNM) model for real color image denoising, where a weight matrix is introduced to exploit the correlated information and noise difference among channels. In the same spirit of MC-WNNM [30], Huang et al. [31] also employed the multi-channel strategy and proposed a multi-channel WSNM (MC-WSNM) model for real color image denoising. However, from the perspective of tensor unfolding, the concatenation CIR methods just utilize one unfolding matrix and ignore the other two unfolding matrices. According to the analyses above, a key challenge for CIR lies in preserving the channel correlations, and the above-mentioned CIR strategies fail to make full use of the correlation information among three color channels, thus the recovered results are often unsatisfactory in terms of reducing the color distortions and color artifacts.

As a new color image representation tool, quaternion encodes the color image pixel into three imaginary parts, which perfectly fits the color image structure and is capable of fully preserving the inter-relationship between the color channels. In very recent years, quaternion-based approaches have been attracting much attention attributing to its rapid development in both theory and applications. Typically, Chen et al. [32] extended LRMA into the quaternion domain and proposed the low rank quaternion approximation (LRQA) for color image denoising and inpainting. Liu et al. [33] combined the quaternion-based TV and sparse dictionary learning for color image super-resolution. Miao et al. [34] developed an efficient low-rank quaternion matrix completion algorithm to recover missing data of a color image and both the LRMF and NNM techniques were combined in their quaternion matrix-based model. Zou et al. [35] proposed a quaternion collaborative and sparse representation model with application to color face recognition. Yu et al. [36] extended the nonlocal patch-based WNNM into quaternion domain and proposed the quaternion-based WNNM method (QWNNM) for color image denoising. Thereafter, Huang et al. [37] proposed a nonlocal patch-based quaternion WNNM model² (QWNNM*) with application to color image deblurring. It is worth mentioning that they are the first to leverage the quaternion representation to address color image deblurring problems. The authors extended the 2-dimensional blurring

² It is denoted as QWNNM* here to avoid confusion with the QWNNM for color image denoising application in [36].

matrix to quaternion domain and correspondingly formulated the quaternion blurring operator. For a comprehensive understanding of the quaternion-based color image processing methods, the interested readers are referred to [38] for more details.

In this paper, on the one hand, as a significant extension, we merge the nonlocal patch-based WSNM into quaternion domain and propose a novel quaternion-based WSNM (QWSNM) model, which is capable of taking advantages of both the WSNM regularizer and quaternion representation for tackling CIR problems. Thanks to the quaternion calculation, the inner-relationship among the color channels can be well preserved. Extensive experiments demonstrate that our proposed QWSNM is superior to many state-of-the-art alternatives, in both the objective evaluation and perceptual observation. To the best of our knowledge, the most similar to our work is the patch-based QWNNM* model proposed by Huang [37] et al., but they did not strictly discuss the convergence behavior of their algorithmic solver. On the other hand, we introduce a unified algorithmic framework to the resulting nonconvex QWNNM* and QWSNM optimization problems. To be specific, by modifying the quaternion ADMM algorithm (QADMM) [39] with a continuation strategy, we theoretically prove that the variable sequences generated by QWNNM* and QWSNM converge to their corresponding stationary points. To facilitate the understanding to readers, Table 1 summarizes the connections and differences between our work and several closely related nonlocal patch-based low rank methods.

Table 1: Comparison of the key attributes between our proposed method and several closely related nonlocal patch-based low rank approaches.

Method	Regularizer term	Task	Quaternion representation	Convergence analysis
WNNM [23]	weighted nuclear norm	grayscale image denoising	✗	✗
WNNM [24]	weighted nuclear norm	color image denoising/inpainting, background subtraction	✗	✓
WSNM [26]	weighted Schatten p -norm	grayscale image denoising, background subtraction	✗	✓
NCW-NNM [27]	weighted Schatten p -norm	color image deblurring/inpainting/compressive sensing	✗	✗
QWNNM [36]	weighted nuclear norm	color image denoising	✓	✗
QWNNM* [37]	weighted nuclear norm	color image deblurring	✓	✗
QWSNM (Proposed)	weighted Schatten p -norm	color image denoising/deblurring	✓	✓

The organization of this paper is as follows. Section 2 briefly reviews several necessary preliminaries, including the basic concepts of quaternion algebra, the QADMM algorithm, nonlocal patch-based QWNNM and WSNM recovery models. Section 3 serves as the main part of this work, where a novel QWSNM model is introduced and the adapted QADMM with a continuation strategy is

developed to solve the resulting nonconvex quaternion minimization problems. Moreover, the convergence analysis of our proposed algorithm is carried out by calculating the residual iteratively for each step of the modified QADMM. In Section 4, we report and discuss the recovery results on color image denoising and color image deblurring by the given method and compare it with several state-of-the-art CIR approaches. Some concluding remarks will be drawn in the Section 5.

2 Preliminaries

In this section, we first briefly review some mathematical notations and definitions of quaternion representation, quaternion algebra and quaternion constrained convex optimization. Then we introduce the WSNM regularization and QWNNM model for CIR. Throughout this paper, scalars, vectors and matrices are denoted as lowercase letters, boldface lowercase letters and boldface capital letters, respectively, e.g., a , \mathbf{a} , \mathbf{A} . Following [36], the variables with a dot above (e.g., \dot{a} , $\dot{\mathbf{a}}$ and $\dot{\mathbf{A}}$) are used to denote the corresponding quaternion variables in the quaternion domain.

2.1 Quaternion Representation and Algebra

As a generalization of the real space \mathbb{R} and complex space \mathbb{C} , the quaternion space is defined as

$$\mathbb{H} = \{a_0 + a_1\mathbf{i} + a_2\mathbf{j} + a_3\mathbf{k} | a_0, a_1, a_2, a_3 \in \mathbb{R}\}, \quad (2)$$

where $\{1, \mathbf{i}, \mathbf{j}, \mathbf{k}\}$ is the basis of \mathbb{H} , and the imaginary units $\mathbf{i}, \mathbf{j}, \mathbf{k}$ obey the quaternion rules $\mathbf{i}^2 = \mathbf{j}^2 = \mathbf{k}^2 = \mathbf{ijk} = -1$, which implies $\mathbf{ij} = \mathbf{k} = -\mathbf{ji}$, $\mathbf{jk} = \mathbf{i} = -\mathbf{kj}$, $\mathbf{ki} = \mathbf{j} = -\mathbf{ik}$.

Let $\dot{a} = a_0 + a_1\mathbf{i} + a_2\mathbf{j} + a_3\mathbf{k} \in \mathbb{H}$, $\dot{b} = b_0 + b_1\mathbf{i} + b_2\mathbf{j} + b_3\mathbf{k} \in \mathbb{H}$, and $\lambda \in \mathbb{R}$, then we have

$$\begin{aligned} \dot{a} + \dot{b} &= (a_0 + b_0) + (a_1 + b_1)\mathbf{i} + (a_2 + b_2)\mathbf{j} + (a_3 + b_3)\mathbf{k}, \\ \lambda\dot{a} &= (\lambda a_0) + (\lambda a_1)\mathbf{i} + (\lambda a_2)\mathbf{j} + (\lambda a_3)\mathbf{k}, \end{aligned} \quad (3)$$

and

$$\begin{aligned} \dot{a}\dot{b} &= (a_0b_0 - a_1b_1 - a_2b_2 - a_3b_3) + (a_0b_1 + a_1b_0 + a_2b_3 - a_3b_2)\mathbf{i} \\ &\quad + (a_0b_2 - a_1b_3 + a_2b_0 + a_3b_1)\mathbf{j} + (a_0b_3 + a_1b_2 - a_2b_1 + a_3b_0)\mathbf{k}. \end{aligned} \quad (4)$$

The conjugate and modulus of \dot{a} are defined by

$$\begin{aligned} \dot{a}^* &= a_0 - a_1\mathbf{i} - a_2\mathbf{j} - a_3\mathbf{k}, \\ |\dot{a}| &= \sqrt{a_0^2 + a_1^2 + a_2^2 + a_3^2}. \end{aligned} \quad (5)$$

The transformation of the quaternion \dot{a} with pure unit quaternions $\mathbf{i}, \mathbf{j}, \mathbf{k}$ is defined as

$$\begin{aligned} \dot{a}^{\mathbf{i}} &= -\mathbf{i}\dot{a}\mathbf{i} = a_0 + a_1\mathbf{i} - a_2\mathbf{j} - a_3\mathbf{k}, \\ \dot{a}^{\mathbf{j}} &= -\mathbf{j}\dot{a}\mathbf{j} = a_0 - a_1\mathbf{i} + a_2\mathbf{j} - a_3\mathbf{k}, \\ \dot{a}^{\mathbf{k}} &= -\mathbf{k}\dot{a}\mathbf{k} = a_0 - a_1\mathbf{i} - a_2\mathbf{j} + a_3\mathbf{k}. \end{aligned} \quad (6)$$

For quaternion matrix $\dot{\mathbf{X}} = (\dot{x}_{ij}) \in \mathbb{H}^{m \times n}$, where $\dot{\mathbf{X}} = \mathbf{X}_0 + \mathbf{X}_1\mathbf{i} + \mathbf{X}_2\mathbf{j} + \mathbf{X}_3\mathbf{k}$, and $\mathbf{X}_l \in \mathbb{R}^{m \times n} (l = 0, 1, 2, 3)$ are real matrices. When $\mathbf{X}_0 = \mathbf{0}$, $\dot{\mathbf{X}}$ reduces to be a pure quaternion matrix. Since color image has three channels (R, G, B), we can represent a color image with a pure quaternion matrix, and the RGB channels of a color image pixel \dot{x}_{ij} can be encoded as three imaginary parts of the quaternion, i.e.,

$$\dot{x}_{ij} = \dot{x}_{ij}^r\mathbf{i} + \dot{x}_{ij}^g\mathbf{j} + \dot{x}_{ij}^b\mathbf{k}, \quad (7)$$

where $i = 1, \dots, m, j = 1, \dots, n$, and $\dot{x}_{ij}^r, \dot{x}_{ij}^g, \dot{x}_{ij}^b \in \mathbb{R}$ are the red, green, blue components at position (i, j) in the color image, respectively.

The quaternion identity matrix $\dot{\mathbf{I}}$ is similar to real-valued identity matrix. For example, if $\dot{\mathbf{I}}_2 \in \mathbb{H}^{2 \times 2}$, it has the form

$$\dot{\mathbf{I}}_2 = \begin{pmatrix} 1 + 0\mathbf{i} + 0\mathbf{j} + 0\mathbf{k} & 0 + 0\mathbf{i} + 0\mathbf{j} + 0\mathbf{k} \\ 0 + 0\mathbf{i} + 0\mathbf{j} + 0\mathbf{k} & 1 + 0\mathbf{i} + 0\mathbf{j} + 0\mathbf{k} \end{pmatrix}, \quad (8)$$

The conjugate operator $\dot{\mathbf{X}}^*$, the transpose operator $\dot{\mathbf{X}}^T$ and the conjugate transpose operator $\dot{\mathbf{X}}^\triangleleft$ are defined as: $\dot{\mathbf{X}}^* = (\dot{x}_{ij}^*)$, $\dot{\mathbf{X}}^T = (\dot{x}_{ji})$ and $\dot{\mathbf{X}}^\triangleleft = (\dot{x}_{ji}^*)$.

The norms of quaternion vectors and matrices are defined as follows [40].

Definition 1 The ℓ_2 -norm of quaternion vector $\dot{\mathbf{a}} = \alpha_0 + \alpha_1\mathbf{i} + \alpha_2\mathbf{j} + \alpha_3\mathbf{k} \in \mathbb{H}^n$ is $\|\dot{\mathbf{a}}\|_2 := \sqrt{\sum_i |\alpha_i|^2}$; the ℓ_2 -norm of quaternion matrix $\dot{\mathbf{X}} = (\dot{x}_{ij})_{m \times n}$

is $\|\dot{\mathbf{X}}\|_2 := \max(\sigma(\dot{\mathbf{X}}))$, where $\sigma(\dot{\mathbf{X}})$ is the set of singular values of $\dot{\mathbf{X}}$; the Frobenius norm of the quaternion matrix $\dot{\mathbf{X}}$ is $\|\dot{\mathbf{X}}\|_F := \sqrt{\sum_{i,j} |\dot{x}_{ij}|^2}$.

Definition 2 (Unitary quaternion matrix) $\dot{\mathbf{X}} \in \mathbb{H}^{m \times m}$ is called unitary quaternion matrix if and only if $\dot{\mathbf{X}}\dot{\mathbf{X}}^\triangleleft = \dot{\mathbf{X}}^\triangleleft\dot{\mathbf{X}} = \dot{\mathbf{I}}_m$, where $\dot{\mathbf{I}}_m$ is the quaternion identity matrix.

The following theorem of quaternion singular value decomposition (QSVD) has been proved by Zhang [41]. Similar to the SVD for real-valued matrices, all the singular values of quaternion matrices are nonnegative and also have the decreasing order property, and the larger singular values contain more color image information.

Theorem 1 (QSVD) Given a quaternion matrix $\dot{\mathbf{Q}} \in \mathbb{H}^{m \times n}$ of rank r , there exist two unitary quaternion matrices $\dot{\mathbf{U}} \in \mathbb{H}^{m \times m}$ and $\dot{\mathbf{V}} \in \mathbb{H}^{n \times n}$ such that $\dot{\mathbf{Q}} = \dot{\mathbf{U}} \begin{pmatrix} \sum_r & 0 \\ 0 & 0 \end{pmatrix} \dot{\mathbf{V}}^*$, where $\sum_r = \text{diag}(\sigma_1, \dots, \sigma_r) \in \mathbb{R}^{r \times r}$, and all singular values $\sigma_i > 0, i = 1, \dots, r$.

Definition 3 (Quaternion rank) The rank of a quaternion matrix is defined as the number of its nonzero singular values.

2.2 QADMM Algorithm

The ADMM is an effective and flexible tool to address many convex and non-convex optimization problems. During the past decades, ADMM has been widely studied and applied in a wealth of applications [42–47]. The basic idea of ADMM is to decompose the original problem into a set of sub-problems and solve them alternately. The ADMM in quaternion domain (QADMM) was first proposed by Flamant et al. [39]. To the following quaternion constraint convex optimization problem

$$\begin{aligned} & \min_{\dot{\mathbf{p}}, \dot{\mathbf{q}}} f(\dot{\mathbf{p}}) + g(\dot{\mathbf{q}}) \\ & s.t. \quad \dot{\mathbf{A}}_1\dot{\mathbf{p}} + \dot{\mathbf{A}}_2\dot{\mathbf{p}}^i + \dot{\mathbf{A}}_3\dot{\mathbf{p}}^j + \dot{\mathbf{A}}_4\dot{\mathbf{p}}^k \\ & \quad + \dot{\mathbf{B}}_1\dot{\mathbf{q}} + \dot{\mathbf{B}}_2\dot{\mathbf{q}}^i + \dot{\mathbf{B}}_3\dot{\mathbf{q}}^j + \dot{\mathbf{B}}_4\dot{\mathbf{q}}^k = \dot{\mathbf{c}}, \end{aligned} \quad (9)$$

where f and g are two convex functions of quaternion variables $\dot{\mathbf{p}} \in \mathbb{H}^n$ and $\dot{\mathbf{q}} \in \mathbb{H}^m$, respectively. The two variables are linked through a widely affine constraint, defined by $\dot{\mathbf{A}}_i \in \mathbb{H}^{p \times n}$, $\dot{\mathbf{B}}_i \in \mathbb{H}^{p \times m}$ for $i = 1, 2, 3, 4$ and $\dot{\mathbf{c}} \in \mathbb{H}^p$.

For the sake of notation brevity, let us define the quaternion residual $r(\dot{\mathbf{p}}, \dot{\mathbf{q}})$ as

$$\begin{aligned} r(\dot{\mathbf{p}}, \dot{\mathbf{q}}) &= \dot{\mathbf{A}}_1 \dot{\mathbf{p}} + \dot{\mathbf{A}}_2 \dot{\mathbf{p}}^i + \dot{\mathbf{A}}_3 \dot{\mathbf{p}}^j + \dot{\mathbf{A}}_4 \dot{\mathbf{p}}^k \\ &+ \dot{\mathbf{B}}_1 \dot{\mathbf{q}} + \dot{\mathbf{B}}_2 \dot{\mathbf{q}}^i + \dot{\mathbf{B}}_3 \dot{\mathbf{q}}^j + \dot{\mathbf{B}}_4 \dot{\mathbf{q}}^k - \dot{\mathbf{c}}. \end{aligned} \quad (10)$$

Thereby, the augmented Lagrangian function of (9) has the form

$$\mathcal{L}_\rho(\dot{\mathbf{p}}, \dot{\mathbf{q}}, \dot{\mathbf{u}}) = f(\dot{\mathbf{p}}) + g(\dot{\mathbf{q}}) + \text{Re}(\dot{\mathbf{u}}^* r(\dot{\mathbf{p}}, \dot{\mathbf{q}})) + \frac{\rho}{2} \|r(\dot{\mathbf{p}}, \dot{\mathbf{q}})\|_2^2, \quad (11)$$

where $\dot{\mathbf{u}}$ denotes the Lagrange multiplier, ρ is the penalty parameter and $\text{Re}(\dot{\mathbf{x}})$ represents the real part of $\dot{\mathbf{x}}$. Similar to the real-valued ADMM [48], the QADMM algorithm consists of the iterations as follows.

$$\begin{cases} \dot{\mathbf{p}}^{(k+1)} = \arg \min_{\dot{\mathbf{p}}} \{f(\dot{\mathbf{p}}) + \frac{\rho}{2} \|r(\dot{\mathbf{p}}, \dot{\mathbf{q}}^{(k)}) + \dot{\mathbf{u}}^{(k)}\|_2^2\}, \\ \dot{\mathbf{q}}^{(k+1)} = \arg \min_{\dot{\mathbf{q}}} \{g(\dot{\mathbf{q}}) + \frac{\rho}{2} \|r(\dot{\mathbf{p}}^{(k+1)}, \dot{\mathbf{q}}) + \dot{\mathbf{u}}^{(k)}\|_2^2\}, \\ \dot{\mathbf{u}}^{(k+1)} = \dot{\mathbf{u}}^{(k)} + r(\dot{\mathbf{p}}^{(k+1)}, \dot{\mathbf{q}}^{(k+1)}). \end{cases} \quad (12)$$

Theorem 2 [39] *Under the assumptions that $f : \mathbb{H}^n \rightarrow \mathbb{R}$ and $g : \mathbb{H}^n \rightarrow \mathbb{R}$ are closed, proper and convex functions, and there exists at least one $(\tilde{\mathbf{p}}, \tilde{\mathbf{q}}, \tilde{\mathbf{u}})$ such that $\mathcal{L}_0(\tilde{\mathbf{p}}, \tilde{\mathbf{q}}, \tilde{\mathbf{u}}) \leq \mathcal{L}_0(\dot{\mathbf{p}}, \tilde{\mathbf{q}}, \tilde{\mathbf{u}}) \leq \mathcal{L}_0(\dot{\mathbf{p}}, \dot{\mathbf{q}}, \tilde{\mathbf{u}})$ for all $\dot{\mathbf{p}}, \dot{\mathbf{q}}, \dot{\mathbf{u}}$, the QADMM algorithm satisfy:*

- *Convergence of the quaternion residual $r(\dot{\mathbf{p}}^{(k)}, \dot{\mathbf{q}}^{(k)}) \rightarrow 0$ as $k \rightarrow \infty$;*
- *Objective convergence: $f(\dot{\mathbf{p}}^{(k)}) + g(\dot{\mathbf{q}}^{(k)}) \rightarrow \tilde{v}$, where \tilde{v} is the optimal value of (9);*
- *Dual variable convergence: $\dot{\mathbf{u}}^{(k)} \rightarrow \tilde{\mathbf{u}}$ as $k \rightarrow \infty$.*

2.3 QWNNM for Color Image Denoising/Deblurring

Although WNNM [24] has achieved excellent performance for grayscale image denoising, it is likely to generate color distortions and color artifacts in the scenarios of color image denoising, since it ignores the inter-relationship among the RGB channels. By leveraging the effective quaternion representation for color images, Yu et al. [36] merged the quaternion representation into WNNM and proposed an effective QWNNM model for color image denoising. Thereafter, Huang et al. [37] extended the QWNNM to color image deblurring.

$$\min_{\dot{\mathbf{X}}} \frac{\lambda}{2} \|\dot{\mathbf{A}}\dot{\mathbf{X}} - \dot{\mathbf{Y}}\|_F^2 + \|\dot{\mathbf{X}}\|_{\mathbf{w},*}, \quad (13)$$

where $\dot{\mathbf{X}} \in \mathbb{H}^{m \times n}$ and $\dot{\mathbf{Y}} \in \mathbb{H}^{m \times n}$ are the encoded counterparts of clean image \mathbf{x} and degraded image \mathbf{y} in Eq. (1) with quaternion representation, respectively. $\dot{\mathbf{A}} \in \mathbb{H}^{m \times m}$ is the convolution matrix with quaternion representation. To be specific,

$$\dot{\mathbf{A}} = \begin{pmatrix} \dot{a}_{11} & \dot{a}_{12} & \dots & \dot{a}_{1m} \\ \dot{a}_{21} & \dot{a}_{22} & \dots & \dot{a}_{2m} \\ \vdots & \vdots & \ddots & \vdots \\ \dot{a}_{m1} & \dot{a}_{m2} & \dots & \dot{a}_{mm} \end{pmatrix}, \quad (14)$$

where $\dot{a}_{ij} = \dot{a}_{ij}^r \mathbf{i} + \dot{a}_{ij}^g \mathbf{j} + \dot{a}_{ij}^b \mathbf{k}$ (and $\dot{a}_{ij}^r, \dot{a}_{ij}^g, \dot{a}_{ij}^b \in \mathbb{R}$) denotes a pixel component of 2-dimensional quaternion matrix $\dot{\mathbf{A}} \in \mathbb{H}^{m \times m}$ ($i = 1, \dots, m; j = 1, \dots, m$). It is easy to see that when $\dot{\mathbf{A}}$ is a quaternion identity matrix, it reduces to the color image denoising. $\|\cdot\|_{\mathbf{w},*}$ denotes the QWNNM regularizer, which is defined as

$$\|\dot{\mathbf{X}}\|_{\mathbf{w},*} = \sum_i |w_i \sigma_i(\dot{\mathbf{X}})|, \quad (15)$$

where $\sigma_i(\dot{\mathbf{X}})$ is the i -th singular value of $\dot{\mathbf{X}}$ and the weight w_i is set as:

$$w_i = \frac{c}{\sigma_i(\dot{\mathbf{X}}) + \epsilon}, \quad (16)$$

where c is a compromising constant, and ϵ is a small positive number to prevent denominator from being zero. By introducing an auxiliary quaternion variable $\dot{\mathbf{Z}}$ with the constraint $\dot{\mathbf{X}} = \dot{\mathbf{Z}}$ and Lagrange multiplier $\dot{\eta} \in \mathbb{H}^{m \times n}$, the augmented Lagrangian function of (13) is formulated by

$$\mathcal{L}(\dot{\mathbf{X}}, \dot{\mathbf{Z}}, \dot{\eta}) = \frac{\lambda}{2} \|\dot{\mathbf{A}}\dot{\mathbf{X}} - \dot{\mathbf{Y}}\|_F^2 + \|\dot{\mathbf{Z}}\|_{\mathbf{w},*} + \frac{\beta}{2} \|\dot{\mathbf{X}} - \dot{\mathbf{Z}}\|_F^2 + \langle \dot{\eta}, \dot{\mathbf{X}} - \dot{\mathbf{Z}} \rangle, \quad (17)$$

where $\beta > 0$ is the penalty parameter. The QADMM algorithm can be applied to solving (17) and the iterative scheme is as follows.

$$\begin{cases} \dot{\mathbf{X}}^{(k+1)} = \arg \min_{\dot{\mathbf{X}}} \mathcal{L}(\dot{\mathbf{X}}, \dot{\mathbf{Z}}^{(k)}, \dot{\eta}^{(k)}), \\ \dot{\mathbf{Z}}^{(k+1)} = \arg \min_{\dot{\mathbf{Z}}} \mathcal{L}(\dot{\mathbf{X}}^{(k+1)}, \dot{\mathbf{Z}}, \dot{\eta}^{(k)}), \\ \dot{\eta}^{(k+1)} = \dot{\eta}^{(k)} + (\dot{\mathbf{X}}^{(k+1)} - \dot{\mathbf{Z}}^{(k+1)}). \end{cases} \quad (18)$$

Concretely, for the $\dot{\mathbf{X}}$ -subproblem of (18), according to the first-order optimality condition, it is easy to obtain that

$$(\lambda \dot{\mathbf{A}}^* \dot{\mathbf{A}} + \beta \dot{\mathbf{I}}) \dot{\mathbf{X}}^{(k+1)} = \lambda \dot{\mathbf{A}}^* \dot{\mathbf{Y}} + \beta \dot{\mathbf{Z}}^{(k)} - \dot{\eta}^{(k)}. \quad (19)$$

Under the quaternion periodic boundary condition for $\dot{\mathbf{X}}$, the $\dot{\mathbf{X}}$ -subproblem can be efficiently tackled by the quaternion fast Fourier transform [49].

$$\dot{\mathbf{X}}^{(k+1)} = \mathcal{F}^{-1} \left(\frac{\lambda \mathcal{F}(\dot{\mathbf{A}})^* \circ \mathcal{F}(\dot{\mathbf{Y}}) + \beta \mathcal{F}(\dot{\mathbf{Z}}^k) - \mathcal{F}(\dot{\eta}^{(k)})}{\lambda \mathcal{F}(\dot{\mathbf{A}})^* \circ \mathcal{F}(\dot{\mathbf{A}}) + \beta \mathbf{I}} \right), \quad (20)$$

where \mathcal{F} denotes two-dimensional discrete quaternion Fourier transform, \mathcal{F}^{-1} denotes two-dimensional discrete inverse quaternion Fourier transform, “ \circ ” and “ $-$ ” represent the component-wise multiplication and division.

By excluding the constant, the $\dot{\mathbf{Z}}$ -subproblem can be reformulated as:

$$\dot{\mathbf{Z}}^{(k+1)} = \arg \min_{\dot{\mathbf{Z}}} \|\dot{\mathbf{Z}}\|_{\mathbf{w},*} + \frac{\beta}{2} \|\dot{\mathbf{Z}} - (\dot{\mathbf{X}}^{(k+1)} + \frac{\dot{\eta}^{(k)}}{\beta})\|_F^2. \quad (21)$$

Suppose $\dot{\mathbf{U}}^{(k)} \Sigma^{(k)} \dot{\mathbf{V}}^{(k)*}$ be the QSVD of $\dot{\mathbf{X}}^{(k+1)} + \frac{\dot{\eta}^{(k)}}{\beta}$, where $\Sigma^{(k)} = \text{diag}\{\sigma_1^{(k)}, \sigma_2^{(k)}, \dots, \sigma_r^{(k)}\}$, $r = \min\{m, n\}$, then the $\dot{\mathbf{Z}}$ -subproblem has a closed-form solution as follows.

$$\dot{\mathbf{Z}}^{(k+1)} = \dot{\mathbf{U}}^{(k)} \Delta^{(k)} \dot{\mathbf{V}}^{(k)*}, \quad (22)$$

where $\Delta^{(k)} = \text{diag}\{\delta_1^{(k)}, \delta_2^{(k)}, \dots, \delta_r^{(k)}\}$, and $\delta_i^{(k)} = \max(\sigma_i^{(k)} - \frac{w_i^{(k)}}{\beta}, 0)$.

Remark: Although the QWNNM* [37] has shown very promising performance for color image deblurring, its convergence behavior has not been strictly studied yet. In this paper, as one of the key contributions, we supplement the convergence analysis of QWNNM* (see the Section 3.4 later) by modifying the original QADMM algorithm through a simple continuation strategy, which is formulated by

$$\begin{cases} \dot{\mathbf{X}}^{(k+1)} = \arg \min_{\dot{\mathbf{X}}} \mathcal{L}(\dot{\mathbf{X}}, \dot{\mathbf{Z}}^{(k)}, \dot{\eta}^{(k)}), \\ \dot{\mathbf{Z}}^{(k+1)} = \arg \min_{\dot{\mathbf{Z}}} \mathcal{L}(\dot{\mathbf{X}}^{(k+1)}, \dot{\mathbf{Z}}, \dot{\eta}^{(k)}), \\ \dot{\eta}^{(k+1)} = \dot{\eta}^{(k)} + \beta^{(k)} (\dot{\mathbf{X}}^{(k+1)} - \dot{\mathbf{Z}}^{(k+1)}), \\ \beta^{(k+1)} = \mu \beta^{(k)}, \quad (\mu > 1). \end{cases} \quad (23)$$

It is worth mentioning that in the original QWNNM* algorithm, the penalty parameter $\beta^{(k)}$ is fixed as a constant β in (18), while it is updated monotonously by adopting a continuation strategy $\beta^{(k+1)} = \mu \beta^{(k)}$, $\mu > 1$ in our adapted version (23). This simple modification is vital to guarantee the fixed-point convergence of QWNNM* algorithm.

2.4 WSNM Regularization

In order to enhance the stability and effectiveness of WNNM, Xie et al. [26] introduced a more accurate rank surrogate and firstly proposed the WSNM model for grayscale image denoising.

$$\min_{\mathbf{X}} \frac{\lambda}{2} \|\mathbf{X} - \mathbf{Y}\|_F^2 + \|\mathbf{X}\|_{\mathbf{w}, S_p}^p, \quad (24)$$

where $\lambda > 0$ is the regularization parameter, \mathbf{Y} is the observed image, \mathbf{X} is the latent image to estimate, and $\|\mathbf{X}\|_{\mathbf{w}, S_p}$ denotes the weighted Schatten p -norm of \mathbf{X} , which is defined as

$$\|\mathbf{X}\|_{\mathbf{w}, S_p} = \left(\sum_{i=1}^{\min\{n, m\}} w_i \sigma_i(\mathbf{X})^p \right)^{\frac{1}{p}}, \quad (25)$$

where $\sigma_i(\mathbf{X})$ is the i -th singular value of \mathbf{X} and the weight w_i is assigned as the same as the formula (16). Thereby, the weighted Schatten p -norm of \mathbf{X} with power p has the form

$$\|\mathbf{X}\|_{\mathbf{w}, S_p}^p = \sum_{i=1}^{\min\{n, m\}} w_i \sigma_i(\mathbf{X})^p. \quad (26)$$

It is obvious to see that WNNM [23] is a special case of WSNM when power $p = 1$. WSNM generalizes WNNM and has more flexibility than WNNM. Moreover, it has been verified experimentally that WSNM outperforms WNNM under different noise levels [26]. Due to the fact that the WSNM is superior to the WNNM for a higher accuracy in signal recovery while theoretically requiring only a weaker restricted isometry property [50], the WSNM regularization has been widely employed in various image processing applications [27, 51, 52].

However, for the complicated CIR tasks, it should be mentioned that all these WSNM methods address the color images in a monochromatic way. More precisely, these WSNM methods treat the RGB channels as three independent “grayscale” images and ignore the important correlations between them. In the next section, we will represent the color image as a pure quaternion matrix and extend the WSNM to the quaternion domain, which is capable of fully preserving the cross-channel correlations of color images and yielding much better CIR recovery results.

3 The Proposed Model and Algorithmic Solver

In this section, we introduce a novel quaternion-based WSNM model (QWSNM) for CIR, after which the corresponding numerical algorithm is also presented. Moreover, the computational complexity of the proposed algorithm is discussed. Finally, the convergence analysis of our new algorithmic solver is given to the QWNNM* [37] and the proposed QWSNM models.

3.1 QWSNM Recovery Model

By combining the benefits of quaternion representation and WSNM regularization, we put forward the QWSNM recovery model for CIR as follows.

$$\min_{\dot{\mathbf{X}}} \frac{\lambda}{2} \|\dot{\mathbf{A}}\dot{\mathbf{X}} - \dot{\mathbf{Y}}\|_F^2 + \|\dot{\mathbf{X}}\|_{\mathbf{w}, S_p}^p, \quad (27)$$

where $\dot{\mathbf{A}} \in \mathbb{H}^{m \times m}$ is the 2-dimensional quaternion degradation matrix, $\dot{\mathbf{X}} \in \mathbb{H}^{m \times n}$ is the original image with quaternion representation, $\dot{\mathbf{Y}} \in \mathbb{H}^{m \times n}$ is the degraded image with quaternion representation, and $\|\cdot\|_{\mathbf{w}, S_p}^p$ is the weighted Schatten p -norm with power p defined the same as the formula (26) presents. Particularly, in the case of color image denoising, our QWSNM model (27) reduces to:

$$\min_{\dot{\mathbf{X}}} \frac{\lambda}{2} \|\dot{\mathbf{X}} - \dot{\mathbf{Y}}\|_F^2 + \|\dot{\mathbf{X}}\|_{\mathbf{w}, S_p}^p. \quad (28)$$

Unlike the QWNNM for color image denoising, it should be mentioned that though the optimization problem (28) no longer has a closed-form solution, it can be well solved by the generalized soft-thresholding (GST) algorithm [53], which will be discussed in detail in the next subsection.

3.2 Algorithmic Solver

To make our formulated model (27) tractable and robust, we also resort to the QADMM iterative scheme to tackle the optimization problem (27). By introducing an auxiliary quaternion variable $\dot{\mathbf{Z}}$ with the constraint $\dot{\mathbf{X}} = \dot{\mathbf{Z}}$, and Lagrange multiplier $\dot{\eta} \in \mathbb{H}^{m \times n}$, the augmented Lagrangian function of (27) is formulated by

$$\mathcal{L}(\dot{\mathbf{X}}, \dot{\mathbf{Z}}, \dot{\eta}) = \frac{\lambda}{2} \|\dot{\mathbf{A}}\dot{\mathbf{X}} - \dot{\mathbf{Y}}\|_F^2 + \|\dot{\mathbf{Z}}\|_{\mathbf{w}, S_p}^p + \frac{\beta}{2} \|\dot{\mathbf{X}} - \dot{\mathbf{Z}}\|_F^2 + \langle \dot{\eta}, \dot{\mathbf{X}} - \dot{\mathbf{Z}} \rangle, \quad (29)$$

where $\beta > 0$ is the penalty parameter. Different from the standard QADMM, a continuation strategy for the penalty parameter is adopted for solving (29):

$$\begin{cases} \dot{\mathbf{X}}^{(k+1)} = \arg \min_{\dot{\mathbf{X}}} \mathcal{L}(\dot{\mathbf{X}}, \dot{\mathbf{Z}}^{(k)}, \dot{\eta}^{(k)}), \\ \dot{\mathbf{Z}}^{(k+1)} = \arg \min_{\dot{\mathbf{Z}}} \mathcal{L}(\dot{\mathbf{X}}^{(k+1)}, \dot{\mathbf{Z}}, \dot{\eta}^{(k)}), \\ \dot{\eta}^{(k+1)} = \dot{\eta}^{(k)} + \beta^{(k)} (\dot{\mathbf{X}}^{(k+1)} - \dot{\mathbf{Z}}^{(k+1)}), \\ \beta^{(k+1)} = \mu \beta^{(k)}, \quad (\mu > 1). \end{cases} \quad (30)$$

It can be seen that the minimization of Eq. (29) involves two separable minimization subproblems, *i.e.*, $\dot{\mathbf{X}}$ and $\dot{\mathbf{Z}}$ subproblems. Next, we will show that each subproblem can be efficiently addressed. To avoid confusion, the subscribe k will be omitted in the following for conciseness.

The $\dot{\mathbf{X}}$ -subproblem is written as:

$$\dot{\mathbf{X}} = \arg \min_{\dot{\mathbf{X}}} \frac{\lambda}{2} \|\dot{\mathbf{A}}\dot{\mathbf{X}} - \dot{\mathbf{Y}}\|_F^2 + \frac{\beta}{2} \|\dot{\mathbf{X}} - \dot{\mathbf{Z}}\|_F^2 + \langle \dot{\eta}, \dot{\mathbf{X}} - \dot{\mathbf{Z}} \rangle. \quad (31)$$

According to the theory of quaternion matrix derivatives [54], Eq. (31) obtains a closed-form solution by derivating the objective function and its solution is expressed as

$$\dot{\mathbf{X}} = (\lambda \dot{\mathbf{A}}^* \dot{\mathbf{A}} + \beta \dot{\mathbf{I}})^{-1} (\lambda \dot{\mathbf{A}}^* \dot{\mathbf{Y}} + \beta \dot{\mathbf{Z}} - \dot{\eta}). \quad (32)$$

For color image deblurring, under the quaternion periodic boundary of $\dot{\mathbf{X}}$, we can utilize the quaternion fast Fourier transform [49] to efficiently solve the Eq. (32).

According to Eq. (30), the $\dot{\mathbf{Z}}$ -subproblem can be equivalently rewritten as:

$$\dot{\mathbf{Z}} = \arg \min_{\dot{\mathbf{Z}}} \|\dot{\mathbf{Z}}\|_{\mathbf{w}, S_p}^p + \frac{\beta}{2} \left\| \dot{\mathbf{Z}} - \left(\dot{\mathbf{X}} + \frac{\dot{\eta}}{\beta} \right) \right\|_F^2. \quad (33)$$

The $\dot{\mathbf{Z}}$ -subproblem coincides to a color image denoising task of $\dot{\mathbf{X}} + \frac{\dot{\eta}}{\beta}$. To utilize the NSS prior in the quaternion space, we first divide the noisy image $\dot{\mathbf{X}} + \frac{\dot{\eta}}{\beta}$ into overlapped patches of size $w \times w$ and assign a number of key patches with a fixed interval as reference. For each key patch, we find its M most similar patches, including itself, in a search window around it (the size of search window is $W \times W$). Then we vectorize the M patches as quaternion column vectors and stack them together to form a quaternion matrix, which is denoted as $\dot{\mathbf{P}}_j \in \mathbb{H}^{w^2 \times M}$. As such, we will get the following optimization

problem.

$$\dot{\mathbf{Z}}_j = \arg \min_{\dot{\mathbf{Z}}_j} \|\dot{\mathbf{Z}}_j\|_{\mathbf{w}, S_p}^p + \frac{\beta}{2} \|\dot{\mathbf{Z}}_j - \dot{\mathbf{P}}_j\|_F^2, \quad (34)$$

where $\dot{\mathbf{Z}}_j \in \mathbb{H}^{w^2 \times M}$ is the nonlocal patch-based quaternion matrix of the clean color image. In this way, we can employ the LRMA methods to estimate the underlying clean patch from its noisy observation. We give the following lemma and theorem to solve the problem (34).

Lemma 1 (Von Neumanns trace inequality [55]) *For any two quaternion matrices $\dot{\mathbf{X}}, \dot{\mathbf{Y}} \in \mathbb{H}^{w^2 \times M}$, $\text{tr}(\dot{\mathbf{X}}^T \dot{\mathbf{Y}}) \leq \text{tr}(\sigma(\dot{\mathbf{X}})^T \sigma(\dot{\mathbf{Y}}))$, where $\sigma(\dot{\mathbf{X}})$ and $\sigma(\dot{\mathbf{Y}})$ are the ordered singular value matrices of $\dot{\mathbf{X}}$ and $\dot{\mathbf{Y}}$ with the same order, respectively.*

Theorem 3 *Let $\dot{\mathbf{U}}_j \Sigma_j \dot{\mathbf{V}}_j^*$ be the QSVD of $\dot{\mathbf{P}}_j$ with $\Sigma_j = \text{diag}(\sigma_{1j}, \dots, \sigma_{rj})$, $r = \min(w^2, M)$. Suppose that all the singular values are in non-ascending order, then the optimal of (34) will be $\dot{\mathbf{Z}}_j = \dot{\mathbf{U}}_j \Delta_j \dot{\mathbf{V}}_j^*$ with $\Delta_j = \text{diag}(\delta_{1j}, \dots, \delta_{rj})$, where δ_{ij} is given by solving the problems below:*

$$\begin{cases} \min_{\delta_{1j}, \dots, \delta_{rj}} \sum_{i=1}^r [(\delta_{ij} - \sigma_{ij})^2 + w_{ij} \delta_{ij}^p], \\ \text{s.t. } \delta_{ij} \geq 0, \text{ and } \delta_{ij} \geq \delta_{kj}, \text{ for } i \leq k. \end{cases} \quad (35)$$

Proof Let the optimal solution of (34) have the QSVD $\dot{\mathbf{Z}}_j = \dot{\mathbf{Q}}_j \Delta_j \dot{\mathbf{R}}_j^*$, and the QSVD of matrix $\dot{\mathbf{P}}_j = \dot{\mathbf{U}}_j \Sigma_j \dot{\mathbf{V}}_j^*$, where both Δ_j and Σ_j are diagonal matrices with the same order (no-ascending). According to Lemma 1, we have

$$\begin{aligned} \|\dot{\mathbf{Z}}_j - \dot{\mathbf{P}}_j\|_F^2 &= \text{tr}(\Delta_j^T \Delta_j) + \text{tr}(\Sigma_j^T \Sigma_j) - 2\text{tr}(\dot{\mathbf{Z}}_j^T \dot{\mathbf{P}}_j) \\ &\leq \text{tr}(\Delta_j^T \Delta_j) + \text{tr}(\Sigma_j^T \Sigma_j) - 2\text{tr}(\Delta_j^T \Sigma_j) \\ &= \|\Delta_j - \Sigma_j\|_F^2, \end{aligned} \quad (36)$$

where the equality holds only when $\dot{\mathbf{Q}}_j = \dot{\mathbf{U}}_j$ and $\dot{\mathbf{R}}_j = \dot{\mathbf{V}}_j$, and the optimal solution of (34) is obtained by solving (35). ■

Therefore, based on Theorem 2, Eq. (34) can be transformed into solving Eq. (35). To obtain the solution of Eq. (35) efficiently, the generalized soft-thresholding (GST) algorithm [53] (see **Algorithm 1** later for details) can be adopted. In particular, given p , σ_{ij} and w_{ij} , there exists a specific threshold:

$$\tau_p^{GST}(w_{ij}) = (2w_{ij}(1-p))^{\frac{1}{2-p}} + w_{ij}p(2w_{ij}(1-p))^{\frac{p-1}{2-p}}. \quad (37)$$

Here if $\sigma_{ij} < \tau_p^{GST}(w_{ij})$, $\delta_{ij} = 0$; otherwise, for any $\sigma_{ij} \in (\tau_p^{GST}(w_{ij}), +\infty)$, Eq. (35) has one unique minimum $S_p^{GST}(\sigma_{ij}; w_{ij})$, which can be solved by the following equation.

$$S_p^{GST}(\sigma_{ij}; w_{ij}) - \sigma_{ij} + w_{ij}p(S_p^{GST}(\sigma_{ij}; w_{ij}))^{p-1} = 0. \quad (38)$$

As a consequence, we can get the closed-form solution of Eq. (35) by the GST algorithm. Based on the denoised patch $\dot{\mathbf{Z}}_j$, we compute the average of repeated estimates for each patch and aggregate all patches together, reconstructing the final clean image $\dot{\mathbf{Z}}$. For the update of the Lagrange penalty parameter β , the continuation strategy is also utilized the same as the adapted version of QWNNM* (25) presents, which is vital to guarantee the convergence of our algorithm. Concluding the above analyses, the whole optimization scheme is summarized in **Algorithm 2**.

3.3 Computational Complexity

In this subsection, we discuss the computational complexity of the proposed QWSNM algorithm. For color image deblurring, the main computational cost of the subproblem $\dot{\mathbf{X}}$ concentrates on computing quaternion fast Fourier transform, and the complexity is $\mathcal{O}(mn \log(mn))$. The time for computing the subproblem $\dot{\mathbf{Z}}$ is mainly consumed by QSVD, and the complexity is $\mathcal{O}(w^4 M)$. The computational cost of GST algorithm in subproblem $\dot{\mathbf{Z}}$ is $\mathcal{O}(JM)$, where J is the inner iteration number of GST algorithm. The computational cost of the Lagrange multiplier $\dot{\eta}$ is $\mathcal{O}(mn)$. Suppose the outer iteration number is K and the number of the patch group in the subproblem $\dot{\mathbf{Z}}$ is N , thus, the total computational cost of the overall optimization algorithm is $\mathcal{O}(K(mn \log(mn) + N(w^4 M + JM) + mn))$. Analogously, the main computation cost of QWSNM for color image denoising is $\mathcal{O}(KNM(w^4 + J))$.

3.4 Convergence Study

In this subsection, we will analyze the convergence of previous QWNNM* (with a continuation strategy) [37] and the proposed Algorithm 2. Due to the non-convexity of QWNNM* model and the proposed QWSNM model, making

Algorithm 1 Generalized soft-thresholding (GST) algorithm

Input: $w_{ij}, \sigma_{ij}, p, J$;
Output: $S_p^{GST}(\sigma_{ij}; w_{ij})$;

- 1: **for** $i = 1, 2, \dots, r$ **do**
- 2: $\tau_p^{GST}(w_{ij}) = (2w_{ij}(1-p))^{\frac{1}{2-p}} + w_{ij}p(2w_{ij}(1-p))^{\frac{p-1}{2-p}}$;
- 3: **if** $|\sigma_{ij}| \leq \tau_p^{GST}(w_{ij})$ **then**
- 4: $S_p^{GST}(\sigma_{ij}; w_{ij}) = 0$;
- 5: **else**
- 6: $s = 0, \delta_{ij}^{(s)} = |\sigma_{ij}|$;
- 7: **for** $s = 0, 1, \dots, J-1$ **do**
- 8: $\delta_{ij}^{(s+1)} = |\sigma_{ij}| - w_{ij}p(\delta_{ij}^{(s)})^{p-1}$;
- 9: **end for**
- 10: $S_p^{GST}(\sigma_{ij}; w_{ij}) = \text{sgn}(\sigma_{ij})\delta_{ij}$;
- 11: **end if**
- 12: **end for**
- 13: **return** $S_p^{GST}(\sigma_{ij}; w_{ij})$.

Algorithm 2 The proposed QWSNM algorithm

Input: Initialize $\dot{\mathbf{X}}^{(0)} = \dot{\mathbf{Y}}, \dot{\mathbf{Z}}^{(0)} = \dot{\mathbf{X}}^{(0)}, \dot{\eta}^{(0)} = 0$; Set parameters λ, β, K ;
Output: The recovered image $\dot{\mathbf{X}}^{(K)}$;

- 1: **for** $k = 0, 1, \dots, K-1$ **do**
- 2: Calculate $\dot{\mathbf{X}}^{(k+1)}$ by solving Eq. (31);
- 3: Calculate $\dot{\mathbf{Z}}^{(k+1)}$ by solving Eq. (33);
- 4: Update $\dot{\eta}^{(k+1)} = \dot{\eta}^{(k)} + \beta^{(k)}(\dot{\mathbf{X}}^{(k+1)} - \dot{\mathbf{Z}}^{(k+1)})$;
- 5: Update $\beta^{(k+1)} = \mu\beta^{(k)}$. \triangleright : (*Continuation strategy*)
- 6: **end for**
- 7: **return** The recovered image $\dot{\mathbf{X}}^{(K)}$.

the convergence analysis become much more challenging, one also should expect a weaker form of convergence. In the following, we provide a fixed-point convergence guarantee of the developed iterative schemes.

Theorem 4 *Assume that the sequence of parameter $\{\beta^{(k)}\}$ is unbounded, then the sequences $\{\dot{\mathbf{X}}^{(k)}\}$ and $\{\dot{\mathbf{Z}}^{(k)}\}$ generated by QWNNM* [37] with a continuation strategy must satisfy the following:*

$$\begin{aligned}
\lim_{k \rightarrow +\infty} \|\dot{\mathbf{X}}^{(k+1)} - \dot{\mathbf{Z}}^{(k+1)}\|_F &= 0, \\
\lim_{k \rightarrow +\infty} \|\dot{\mathbf{X}}^{(k+1)} - \dot{\mathbf{X}}^{(k)}\|_F &= 0, \\
\lim_{k \rightarrow +\infty} \|\dot{\mathbf{Z}}^{(k+1)} - \dot{\mathbf{Z}}^{(k)}\|_F &= 0.
\end{aligned} \tag{39}$$

Proof We first prove that the sequence $\{\dot{\eta}^{(k)}\}$ generated by QWNNM* with a continuation strategy is upper bounded. Suppose $\dot{\mathbf{P}}^{(k)} = \frac{1}{\beta^{(k)}}\dot{\eta}^{(k)} + \dot{\mathbf{X}}^{(k+1)}$, then we can get N patch-based quaternion matrices $\dot{\mathbf{P}}_j^{(k)}$ and N patch-based quaternion matrices $\dot{\mathbf{Z}}_j^{(k+1)}$ ($j = 1, 2, \dots, N$) by utilizing the NSS prior. Denote the QSVD of patch-based quaternion matrix $\dot{\mathbf{P}}_j^{(k)}$ in the $k + 1$ iteration as $\dot{\mathbf{U}}_j^{(k)} \Sigma_j^{(k)} \dot{\mathbf{V}}_j^{(k)*}$, where $\Sigma_j^{(k)} = \text{diag}(\sigma_{1j}^{(k)}, \sigma_{2j}^{(k)}, \dots, \sigma_{rj}^{(k)})$ is the diagonal singular value matrix. According the formula (22), we have $\dot{\mathbf{Z}}_j^{(k+1)} = \dot{\mathbf{U}}_j^{(k)} \Delta_j^{(k)} \dot{\mathbf{V}}_j^{(k)*}$, where $\Delta_j^{(k)} = \text{diag}(\delta_{1j}^{(k)}, \delta_{2j}^{(k)}, \dots, \delta_{rj}^{(k)})$ is the singular value matrix. Then

$$\begin{aligned} \|\dot{\eta}^{(k+1)}\|_F^2 &= \|\dot{\eta}^{(k)} + \beta^{(k)}(\dot{\mathbf{X}}^{(k+1)} - \dot{\mathbf{Z}}^{(k+1)})\|_F^2 \\ &\leq (\beta^{(k)})^2 \sum_{j=1}^N \|\dot{\mathbf{U}}_j^{(k)} \Sigma_j^{(k)} \dot{\mathbf{V}}_j^{(k)*} - \dot{\mathbf{U}}_j^{(k)} \Delta_j^{(k)} \dot{\mathbf{V}}_j^{(k)*}\|_F^2 \\ &= (\beta^{(k)})^2 \sum_{j=1}^N \|\Sigma_j^{(k)} - \Delta_j^{(k)}\|_F^2 \leq \sum_{j=1}^N \sum_i (w_{ij}^{(k)})^2. \end{aligned} \quad (40)$$

Hence, the sequence $\{\dot{\eta}^{(k)}\}$ generated by QWNNM* is upper bounded.

We then prove that the sequence of the Lagrange function $\{\mathcal{L}(\dot{\mathbf{X}}^{(k+1)}, \dot{\mathbf{Z}}^{(k+1)}, \dot{\eta}^{(k+1)}, \beta^{(k+1)})\}$ is also upper bounded. Due to the updating rule of $\dot{\eta}$, we can get

$$\begin{aligned} &\mathcal{L}(\dot{\mathbf{X}}^{(k+1)}, \dot{\mathbf{Z}}^{(k+1)}, \dot{\eta}^{(k+1)}, \beta^{(k+1)}) \\ &= \|\dot{\mathbf{A}}\dot{\mathbf{X}}^{(k+1)} - \dot{\mathbf{Y}}\|_F^2 + \|\dot{\mathbf{Z}}^{(k+1)}\|_{\mathbf{w},*} \\ &+ \left\langle \dot{\eta}^{(k+1)}, \dot{\mathbf{X}}^{(k+1)} - \dot{\mathbf{Z}}^{(k+1)} \right\rangle + \frac{\beta^{(k+1)}}{2} \|\dot{\mathbf{X}}^{(k+1)} - \dot{\mathbf{Z}}^{(k+1)}\|_F^2 \\ &= \mathcal{L}(\dot{\mathbf{X}}^{(k+1)}, \dot{\mathbf{Z}}^{(k+1)}, \dot{\eta}^{(k)}, \beta^{(k)}) \\ &+ \left\langle \dot{\eta}^{(k+1)} - \dot{\eta}^{(k)}, \dot{\mathbf{X}}^{(k+1)} - \dot{\mathbf{Z}}^{(k+1)} \right\rangle + \frac{\beta^{(k+1)} - \beta^{(k)}}{2} \|\dot{\mathbf{X}}^{(k+1)} - \dot{\mathbf{Z}}^{(k+1)}\|_F^2 \\ &= \mathcal{L}(\dot{\mathbf{X}}^{(k+1)}, \dot{\mathbf{Z}}^{(k+1)}, \dot{\eta}^{(k)}, \beta^{(k)}) \\ &+ \left\langle \dot{\eta}^{(k+1)} - \dot{\eta}^{(k)}, \frac{\dot{\eta}^{(k+1)} - \dot{\eta}^{(k)}}{\beta^{(k)}} \right\rangle + \frac{\beta^{(k+1)} - \beta^{(k)}}{2} \left\| \frac{\dot{\eta}^{(k+1)} - \dot{\eta}^{(k)}}{\beta^{(k)}} \right\|_F^2 \\ &= \mathcal{L}(\dot{\mathbf{X}}^{(k+1)}, \dot{\mathbf{Z}}^{(k+1)}, \dot{\eta}^{(k)}, \beta^{(k)}) + \frac{\beta^{(k+1)} + \beta^{(k)}}{2(\beta^{(k)})^2} \|\dot{\eta}^{(k+1)} - \dot{\eta}^{(k)}\|_F^2. \end{aligned} \quad (41)$$

Since $\{\dot{\eta}^{(k)}\}$ is upper bounded, the sequence $\{\dot{\eta}^{(k+1)} - \dot{\eta}^{(k)}\}$ is also upper bounded. Suppose M_0 is the upper bound of $\{\dot{\eta}^{(k+1)} - \dot{\eta}^{(k)}\}$ for all $k \geq 0$, i.e., $\|\dot{\eta}^{(k+1)} - \dot{\eta}^{(k)}\|_F^2 \leq M_0^2, \forall k \geq 0$. Besides, the inequality $\mathcal{L}(\dot{\mathbf{X}}^{(k+1)}, \dot{\mathbf{Z}}^{(k+1)}, \dot{\eta}^{(k)},$

$\beta^{(k)} \leq \mathcal{L}(\dot{\mathbf{X}}^{(k)}, \dot{\mathbf{Z}}^{(k)}, \dot{\eta}^{(k)}, \beta^{(k)})$ always holds since we have the globally optimal solution of $\dot{\mathbf{X}}$ and $\dot{\mathbf{Z}}$ in their corresponding sub-problems. Therefore, we have

$$\begin{aligned}
\mathcal{L}(\dot{\mathbf{X}}^{(k+1)}, \dot{\mathbf{Z}}^{(k+1)}, \dot{\eta}^{(k+1)}, \beta^{(k+1)}) &\leq \mathcal{L}(\dot{\mathbf{X}}^{(k+1)}, \dot{\mathbf{Z}}^{(k+1)}, \dot{\eta}^{(k)}, \beta^{(k)}) + \frac{\beta^{(k+1)} + \beta^{(k)}}{2(\beta^{(k)})^2} M_0^2 \\
&\leq \mathcal{L}(\dot{\mathbf{X}}^{(1)}, \dot{\mathbf{Z}}^{(1)}, \dot{\eta}^{(0)}, \beta^{(0)}) + M_0^2 \sum_{k=0}^{\infty} \frac{\beta^{(k+1)} + \beta^{(k)}}{2(\beta^{(k)})^2} \\
&= \mathcal{L}(\dot{\mathbf{X}}^{(1)}, \dot{\mathbf{Z}}^{(1)}, \dot{\eta}^{(0)}, \beta^{(0)}) + M_0^2 \sum_{k=0}^{\infty} \frac{1 + \mu}{2\beta^{(0)}\mu^k} \\
&\leq \mathcal{L}(\dot{\mathbf{X}}^{(1)}, \dot{\mathbf{Z}}^{(1)}, \dot{\eta}^{(0)}, \beta^{(0)}) + \frac{M_0^2}{\beta^{(0)}} \sum_{k=0}^{\infty} \frac{1}{\mu^{k-1}} \\
&< +\infty.
\end{aligned} \tag{42}$$

Therefore, $\{\mathcal{L}(\dot{\mathbf{X}}^{(k+1)}, \dot{\mathbf{Z}}^{(k+1)}, \dot{\eta}^{(k+1)}, \beta^{(k+1)})\}$ is upper bounded.

We next prove the sequences of $\{\dot{\mathbf{X}}^{(k)}\}$ and $\{\dot{\mathbf{Z}}^{(k)}\}$ are upper bounded. According to the formula (17), we have

$$\begin{aligned}
&\|\dot{\mathbf{A}}\dot{\mathbf{X}}^{(k+1)} - \dot{\mathbf{Y}}\|_F^2 + \|\dot{\mathbf{Z}}^{(k+1)}\|_{\mathbf{w},*} \\
&= \mathcal{L}(\dot{\mathbf{X}}^{(k)}, \dot{\mathbf{Z}}^{(k)}, \dot{\eta}^{(k-1)}, \beta^{(k-1)}) - \left\langle \dot{\eta}^{(k)}, \dot{\mathbf{X}}^{(k)} - \dot{\mathbf{Z}}^{(k)} \right\rangle - \frac{\beta^{(k-1)}}{2} \|\dot{\mathbf{X}}^{(k)} - \dot{\mathbf{Z}}^{(k)}\|_F^2 \\
&= \mathcal{L}(\dot{\mathbf{X}}^{(k)}, \dot{\mathbf{Z}}^{(k)}, \dot{\eta}^{(k-1)}, \beta^{(k-1)}) - \left\langle \dot{\eta}^{(k-1)}, \frac{\dot{\eta}^{(k)} - \dot{\eta}^{(k-1)}}{\beta^{(k)}} \right\rangle - \frac{\beta^{(k-1)}}{2} \left\| \frac{\dot{\eta}^{(k)} - \dot{\eta}^{(k-1)}}{\beta^{(k)}} \right\|_F^2 \\
&= \mathcal{L}(\dot{\mathbf{X}}^{(k)}, \dot{\mathbf{Z}}^{(k)}, \dot{\eta}^{(k-1)}, \beta^{(k-1)}) + \frac{\|\dot{\eta}^{(k-1)}\|_F^2 - \|\dot{\eta}^{(k)}\|_F^2}{2\beta^{(k-1)}}.
\end{aligned} \tag{43}$$

Then, we can conclude that the sequence $\{\dot{\mathbf{Z}}^{(k)}\}$ is upper bounded. Since $\dot{\eta}^{(k+1)} = \dot{\eta}^{(k)} + \beta^{(k)}(\dot{\mathbf{X}}^{(k+1)} - \dot{\mathbf{Z}}^{(k+1)})$, $\{\dot{\mathbf{X}}^{(k)}\}$ is also upper bounded. Thus, there exists at least one accumulation point for $\{\dot{\mathbf{X}}^{(k)}, \dot{\mathbf{Z}}^{(k)}\}$. Moreover, we obtain that

$$\lim_{k \rightarrow +\infty} \|\dot{\mathbf{X}}^{(k+1)} - \dot{\mathbf{Z}}^{(k+1)}\|_F = \lim_{k \rightarrow +\infty} \frac{1}{\beta^{(k)}} \|\dot{\eta}^{(k+1)} - \dot{\eta}^{(k)}\|_F = 0, \tag{44}$$

and that the accumulation point is a feasible solution to the objective function. Thus, the first equation in (39) is proved.

Finally, we prove that the change of sequence $\{\dot{\mathbf{X}}^{(k)}\}$ and $\{\dot{\mathbf{Z}}^{(k)}\}$ between consecutive iterations tends to be 0. For $\dot{\mathbf{X}}^{(k+1)}$ and $\dot{\mathbf{X}}^{(k)} = \frac{1}{\beta^{(k-1)}}(\dot{\eta}^{(k)} -$

$\dot{\eta}^{(k-1)} + \dot{\mathbf{Z}}^{(k)}$, we have

$$\begin{aligned}
\lim_{k \rightarrow +\infty} \|\dot{\mathbf{X}}^{(k+1)} - \dot{\mathbf{X}}^{(k)}\|_F &= \lim_{k \rightarrow +\infty} \left\| (\lambda \dot{\mathbf{A}}^* \dot{\mathbf{A}} + \beta^{(k)} \dot{\mathbf{I}})^{-1} (\lambda \dot{\mathbf{A}}^* \dot{\mathbf{Y}} + \beta^{(k)} \dot{\mathbf{Z}}^{(k)} - \dot{\eta}^{(k)}) \right. \\
&\quad \left. - \frac{1}{\beta^{(k-1)}} (\dot{\eta}^{(k)} - \dot{\eta}^{(k-1)}) - \dot{\mathbf{Z}}^{(k)} \right\|_F \\
&= \lim_{k \rightarrow +\infty} \left\| (\lambda \dot{\mathbf{A}}^* \dot{\mathbf{A}} + \beta^{(k)} \dot{\mathbf{I}})^{-1} (\lambda \dot{\mathbf{A}}^* \dot{\mathbf{Y}} - \lambda \dot{\mathbf{A}}^* \dot{\mathbf{A}} \dot{\mathbf{Z}}^{(k)} - \dot{\eta}^{(k)}) \right. \\
&\quad \left. - \frac{1}{\beta^{(k-1)}} (\dot{\eta}^{(k)} - \dot{\eta}^{(k-1)}) \right\|_F \\
&\leq \lim_{k \rightarrow +\infty} \left\| (\lambda \dot{\mathbf{A}}^* \dot{\mathbf{A}} + \beta^{(k)} \dot{\mathbf{I}})^{-1} (\lambda \dot{\mathbf{A}}^* \dot{\mathbf{Y}} - \lambda \dot{\mathbf{A}}^* \dot{\mathbf{A}} \dot{\mathbf{Z}}^{(k)} - \dot{\eta}^{(k)}) \right\|_F \\
&\quad + \frac{1}{\beta^{(k-1)}} \|\dot{\eta}^{(k)} - \dot{\eta}^{(k-1)}\|_F = 0.
\end{aligned} \tag{45}$$

Since $\dot{\mathbf{Z}}^{(k+1)} = \frac{1}{\beta^{(k)}} \dot{\eta}^{(k)} - \frac{1}{\beta^{(k)}} \dot{\eta}^{(k+1)} + \dot{\mathbf{X}}^{(k+1)}$, we conclude that

$$\begin{aligned}
\lim_{k \rightarrow +\infty} \|\dot{\mathbf{Z}}^{(k+1)} - \dot{\mathbf{Z}}^{(k)}\|_F &= \lim_{k \rightarrow +\infty} \left\| \frac{1}{\beta^{(k)}} \dot{\eta}^{(k)} - \frac{1}{\beta^{(k)}} \dot{\eta}^{(k+1)} + \dot{\mathbf{X}}^{(k+1)} - \dot{\mathbf{Z}}^{(k)} \right\|_F \\
&= \lim_{k \rightarrow +\infty} \left\| \dot{\mathbf{X}}^{(k)} + \frac{1}{\beta^{(k-1)}} \dot{\eta}^{(k-1)} - \dot{\mathbf{Z}}^{(k)} + \dot{\mathbf{X}}^{(k+1)} \right. \\
&\quad \left. - \dot{\mathbf{X}}^{(k)} - \frac{1}{\beta^{(k-1)}} \dot{\eta}^{(k-1)} + \frac{1}{\beta^{(k)}} \dot{\eta}^{(k)} - \frac{1}{\beta^{(k)}} \dot{\eta}^{(k+1)} \right\|_F \\
&\leq \lim_{k \rightarrow +\infty} \sum_{j=1}^N \left\| \sum_i w_{ij}^{(k-1)} / \beta^{(k-1)} \right\|_F + \|\dot{\mathbf{X}}^{(k+1)} - \dot{\mathbf{X}}^{(k)}\|_F \\
&\quad + \left\| \frac{1}{\beta^{(k-1)}} \dot{\eta}^{(k-1)} - \frac{1}{\beta^{(k)}} \dot{\eta}^{(k)} + \frac{1}{\beta^{(k)}} \dot{\eta}^{(k+1)} \right\|_F = 0.
\end{aligned} \tag{46}$$

This completes the proof. ■

Theorem 5 Assume that the sequence of parameter $\{\beta^{(k)}\}$ is unbounded, then the sequences $\{\dot{\mathbf{X}}^{(k)}\}$ and $\{\dot{\mathbf{Z}}^{(k)}\}$ generated by Algorithm 2 must satisfy the following:

$$\begin{aligned}
\lim_{k \rightarrow +\infty} \|\dot{\mathbf{X}}^{(k+1)} - \dot{\mathbf{Z}}^{(k+1)}\|_F &= 0, \\
\lim_{k \rightarrow +\infty} \|\dot{\mathbf{X}}^{(k+1)} - \dot{\mathbf{X}}^{(k)}\|_F &= 0, \\
\lim_{k \rightarrow +\infty} \|\dot{\mathbf{Z}}^{(k+1)} - \dot{\mathbf{Z}}^{(k)}\|_F &= 0.
\end{aligned} \tag{47}$$

Proof We first prove that the sequence $\{\dot{\eta}^{(k)}\}$ generated by Algorithm 2 is upper bounded. Suppose $\dot{\mathbf{P}}^{(k)} = \frac{1}{\beta^{(k)}} \dot{\eta}^{(k)} + \dot{\mathbf{X}}^{(k+1)}$, then we can get N patch-based quaternion matrices $\dot{\mathbf{P}}_j^{(k)}$ and N patch-based quaternion matrices $\dot{\mathbf{Z}}_j^{(k+1)}$ ($j =$

$1, 2, \dots, N$) by utilizing the NSS prior. Denote the QSVD of patch-based quaternion matrix $\dot{\mathbf{P}}_j^{(k)}$ in the $k+1$ iteration as $\dot{\mathbf{U}}_j^{(k)} \Sigma_j^{(k)} \dot{\mathbf{V}}_j^{(k)*}$, where $\Sigma_j^{(k)} = \text{diag}(\sigma_{1j}^{(k)}, \sigma_{2j}^{(k)}, \dots, \sigma_{rj}^{(k)})$ is the diagonal singular value matrix. By using the GST algorithm for $\dot{\mathbf{Z}}_j$ subproblem, we have $\dot{\mathbf{Z}}_j^{(k+1)} = \dot{\mathbf{U}}_j^{(k)} \Delta_j^{(k)} \dot{\mathbf{V}}_j^{(k)*}$, where $\Delta_j^{(k)} = \text{diag}(\delta_{1j}^{(k)}, \delta_{2j}^{(k)}, \dots, \delta_{rj}^{(k)})$ is the singular value matrix after generalized soft-thresholding operation. Then,

$$\begin{aligned}
\|\dot{\boldsymbol{\eta}}^{(k+1)}\|_F^2 &= \|\dot{\boldsymbol{\eta}}^{(k)} + \beta^{(k)}(\dot{\mathbf{X}}^{(k+1)} - \dot{\mathbf{Z}}^{(k+1)})\|_F^2 \\
&= (\beta^{(k)})^2 \left\| \frac{1}{\beta^{(k)}} \dot{\boldsymbol{\eta}}^{(k)} + \dot{\mathbf{X}}^{(k+1)} - \dot{\mathbf{Z}}^{(k+1)} \right\|_F^2 \\
&\leq (\beta^{(k)})^2 \sum_{j=1}^N \left\| \dot{\mathbf{U}}_j^{(k)} \Sigma_j^{(k)} \dot{\mathbf{V}}_j^{(k)*} - \dot{\mathbf{U}}_j^{(k)} \Delta_j^{(k)} \dot{\mathbf{V}}_j^{(k)*} \right\|_F^2 \\
&= (\beta^{(k)})^2 \sum_{j=1}^N \left\| \Sigma_j^{(k)} - \Delta_j^{(k)} \right\|_F^2 = \sum_{j=1}^N (\beta^{(k)})^2 \left\| \sum_i J w_{ij}^{(k)} / \beta^{(k)} \right\|_F^2 \\
&= \sum_{j=1}^N \left\| J \sum_i w_{ij}^{(k)} \right\|_F^2.
\end{aligned} \tag{48}$$

Hence, the sequence $\{\dot{\boldsymbol{\eta}}^{(k)}\}$ generated by Algorithm 2 is upper bounded.

We then prove that the sequence of the Lagrange function $\{\mathcal{L}(\dot{\mathbf{X}}^{(k+1)}, \dot{\mathbf{Z}}^{(k+1)}, \dot{\boldsymbol{\eta}}^{(k+1)}, \beta^{(k+1)})\}$ is also upper bounded. Due to the updating rule of $\dot{\boldsymbol{\eta}}$, we can get

$$\begin{aligned}
&\mathcal{L}(\dot{\mathbf{X}}^{(k+1)}, \dot{\mathbf{Z}}^{(k+1)}, \dot{\boldsymbol{\eta}}^{(k+1)}, \beta^{(k+1)}) \\
&= \|\dot{\mathbf{A}} \dot{\mathbf{X}}^{(k+1)} - \dot{\mathbf{Y}}\|_F^2 + \|\dot{\mathbf{Z}}^{(k+1)}\|_{\mathbf{w}, S_p}^p \\
&+ \left\langle \dot{\boldsymbol{\eta}}^{(k+1)}, \dot{\mathbf{X}}^{(k+1)} - \dot{\mathbf{Z}}^{(k+1)} \right\rangle + \frac{\beta^{(k+1)}}{2} \|\dot{\mathbf{X}}^{(k+1)} - \dot{\mathbf{Z}}^{(k+1)}\|_F^2 \\
&= \mathcal{L}(\dot{\mathbf{X}}^{(k+1)}, \dot{\mathbf{Z}}^{(k+1)}, \dot{\boldsymbol{\eta}}^{(k)}, \beta^{(k)}) \\
&+ \left\langle \dot{\boldsymbol{\eta}}^{(k+1)} - \dot{\boldsymbol{\eta}}^{(k)}, \dot{\mathbf{X}}^{(k+1)} - \dot{\mathbf{Z}}^{(k+1)} \right\rangle + \frac{\beta^{(k+1)} - \beta^{(k)}}{2} \|\dot{\mathbf{X}}^{(k+1)} - \dot{\mathbf{Z}}^{(k+1)}\|_F^2 \\
&= \mathcal{L}(\dot{\mathbf{X}}^{(k+1)}, \dot{\mathbf{Z}}^{(k+1)}, \dot{\boldsymbol{\eta}}^{(k)}, \beta^{(k)}) \\
&+ \left\langle \dot{\boldsymbol{\eta}}^{(k+1)} - \dot{\boldsymbol{\eta}}^{(k)}, \frac{\dot{\boldsymbol{\eta}}^{(k+1)} - \dot{\boldsymbol{\eta}}^{(k)}}{\beta^{(k)}} \right\rangle + \frac{\beta^{(k+1)} - \beta^{(k)}}{2} \left\| \frac{\dot{\boldsymbol{\eta}}^{(k+1)} - \dot{\boldsymbol{\eta}}^{(k)}}{\beta^{(k)}} \right\|_F^2 \\
&= \mathcal{L}(\dot{\mathbf{X}}^{(k+1)}, \dot{\mathbf{Z}}^{(k+1)}, \dot{\boldsymbol{\eta}}^{(k)}, \beta^{(k)}) + \frac{\beta^{(k+1)} + \beta^{(k)}}{2(\beta^{(k)})^2} \|\dot{\boldsymbol{\eta}}^{(k+1)} - \dot{\boldsymbol{\eta}}^{(k)}\|_F^2.
\end{aligned} \tag{49}$$

Since $\{\dot{\eta}^{(k)}\}$ is upper bounded, the sequence $\{\dot{\eta}^{(k+1)} - \dot{\eta}^{(k)}\}$ is also upper bounded. Suppose M_0 is the upper bound of $\{\dot{\eta}^{(k+1)} - \dot{\eta}^{(k)}\}$ for all $k \geq 0$, i.e., $\|\dot{\eta}^{(k+1)} - \dot{\eta}^{(k)}\|_F^2 \leq M_0^2, \forall k \geq 0$. Besides, the inequality $\mathcal{L}(\dot{\mathbf{X}}^{(k+1)}, \dot{\mathbf{Z}}^{(k+1)}, \dot{\eta}^{(k)}, \beta^{(k)}) \leq \mathcal{L}(\dot{\mathbf{X}}^{(k)}, \dot{\mathbf{Z}}^{(k)}, \dot{\eta}^{(k)}, \beta^{(k)})$ always holds since we have the globally optimal solution of $\dot{\mathbf{X}}$ and $\dot{\mathbf{Z}}$ in their corresponding sub-problems. Therefore, we have

$$\begin{aligned}
\mathcal{L}(\dot{\mathbf{X}}^{(k+1)}, \dot{\mathbf{Z}}^{(k+1)}, \dot{\eta}^{(k+1)}, \beta^{(k+1)}) &\leq \mathcal{L}(\dot{\mathbf{X}}^{(k+1)}, \dot{\mathbf{Z}}^{(k+1)}, \dot{\eta}^{(k)}, \beta^{(k)}) + \frac{\beta^{(k+1)} + \beta^{(k)}}{2(\beta^{(k)})^2} M_0^2 \\
&\leq \mathcal{L}(\dot{\mathbf{X}}^{(1)}, \dot{\mathbf{Z}}^{(1)}, \dot{\eta}^{(0)}, \beta^{(0)}) + M_0^2 \sum_{k=0}^{\infty} \frac{\beta^{(k+1)} + \beta^{(k)}}{2(\beta^{(k)})^2} \\
&= \mathcal{L}(\dot{\mathbf{X}}^{(1)}, \dot{\mathbf{Z}}^{(1)}, \dot{\eta}^{(0)}, \beta^{(0)}) + M_0^2 \sum_{k=0}^{\infty} \frac{1 + \mu}{2\beta^{(0)}\mu^k} \\
&\leq \mathcal{L}(\dot{\mathbf{X}}^{(1)}, \dot{\mathbf{Z}}^{(1)}, \dot{\eta}^{(0)}, \beta^{(0)}) + \frac{M_0^2}{\beta^{(0)}} \sum_{k=0}^{\infty} \frac{1}{\mu^{k-1}} \\
&< +\infty.
\end{aligned} \tag{50}$$

Thus, $\{\mathcal{L}(\dot{\mathbf{X}}^{(k+1)}, \dot{\mathbf{Z}}^{(k+1)}, \dot{\eta}^{(k+1)}, \beta^{(k+1)})\}$ is upper bounded.

We next prove the sequences of $\{\dot{\mathbf{X}}^{(k)}\}$ and $\{\dot{\mathbf{Z}}^{(k)}\}$ are upper bounded. According to the formula (29), we have

$$\begin{aligned}
&\|\dot{\mathbf{A}}\dot{\mathbf{X}}^{(k+1)} - \dot{\mathbf{Y}}\|_F^2 + \|\dot{\mathbf{Z}}^{(k+1)}\|_{\mathbf{w}, S_p}^p \\
&= \mathcal{L}(\dot{\mathbf{X}}^{(k)}, \dot{\mathbf{Z}}^{(k)}, \dot{\eta}^{(k-1)}, \beta^{(k-1)}) - \left\langle \dot{\eta}^{(k)}, \dot{\mathbf{X}}^{(k)} - \dot{\mathbf{Z}}^{(k)} \right\rangle - \frac{\beta^{(k-1)}}{2} \|\dot{\mathbf{X}}^{(k)} - \dot{\mathbf{Z}}^{(k)}\|_F^2 \\
&= \mathcal{L}(\dot{\mathbf{X}}^{(k)}, \dot{\mathbf{Z}}^{(k)}, \dot{\eta}^{(k-1)}, \beta^{(k-1)}) - \left\langle \dot{\eta}^{(k-1)}, \frac{\dot{\eta}^{(k)} - \dot{\eta}^{(k-1)}}{\beta^{(k)}} \right\rangle - \frac{\beta^{(k-1)}}{2} \left\| \frac{\dot{\eta}^{(k)} - \dot{\eta}^{(k-1)}}{\beta^{(k)}} \right\|_F^2 \\
&= \mathcal{L}(\dot{\mathbf{X}}^{(k)}, \dot{\mathbf{Z}}^{(k)}, \dot{\eta}^{(k-1)}, \beta^{(k-1)}) + \frac{\|\dot{\eta}^{(k-1)}\|_F^2 - \|\dot{\eta}^{(k)}\|_F^2}{2\beta^{(k-1)}}.
\end{aligned} \tag{51}$$

Therefore, we can conclude that the sequence $\{\dot{\mathbf{Z}}^{(k)}\}$ is upper bounded. Since $\dot{\eta}^{(k+1)} = \dot{\eta}^{(k)} + \beta^{(k)}(\dot{\mathbf{X}}^{(k+1)} - \dot{\mathbf{Z}}^{(k+1)})$, $\{\dot{\mathbf{X}}^{(k)}\}$ is also upper bounded. Thus, there exists at least one accumulation point for $\{\dot{\mathbf{X}}^{(k)}, \dot{\mathbf{Z}}^{(k)}\}$. Moreover, we obtain that

$$\lim_{k \rightarrow +\infty} \|\dot{\mathbf{X}}^{(k+1)} - \dot{\mathbf{Z}}^{(k+1)}\|_F = \lim_{k \rightarrow +\infty} \frac{1}{\beta^{(k)}} \|\dot{\eta}^{(k+1)} - \dot{\eta}^{(k)}\|_F = 0, \tag{52}$$

and that the accumulation point is a feasible solution to the objective function.

Thus, the first equation in (47) is proved.

Finally, we prove that the change of sequence $\{\dot{\mathbf{X}}^{(k)}\}$ and $\{\dot{\mathbf{Z}}^{(k)}\}$ between consecutive iterations tends to be 0. For $\dot{\mathbf{X}}^{(k+1)}$ and $\dot{\mathbf{X}}^{(k)} = \frac{1}{\beta^{(k-1)}}(\dot{\eta}^{(k)} - \dot{\eta}^{(k-1)}) + \dot{\mathbf{Z}}^{(k)}$, we have

$$\begin{aligned}
\lim_{k \rightarrow +\infty} \|\dot{\mathbf{X}}^{(k+1)} - \dot{\mathbf{X}}^{(k)}\|_F &= \lim_{k \rightarrow +\infty} \left\| (\lambda \dot{\mathbf{A}}^* \dot{\mathbf{A}} + \beta^{(k)} \dot{\mathbf{I}})^{-1} (\lambda \dot{\mathbf{A}}^* \dot{\mathbf{Y}} + \beta^{(k)} \dot{\mathbf{Z}}^{(k)} - \dot{\eta}^{(k)}) \right. \\
&\quad \left. - \frac{1}{\beta^{(k-1)}} (\dot{\eta}^{(k)} - \dot{\eta}^{(k-1)}) - \dot{\mathbf{Z}}^{(k)} \right\|_F \\
&= \lim_{k \rightarrow +\infty} \left\| (\lambda \dot{\mathbf{A}}^* \dot{\mathbf{A}} + \beta^{(k)} \dot{\mathbf{I}})^{-1} (\lambda \dot{\mathbf{A}}^* \dot{\mathbf{Y}} - \lambda \dot{\mathbf{A}}^* \dot{\mathbf{A}} \dot{\mathbf{Z}}^{(k)} - \dot{\eta}^{(k)}) \right. \\
&\quad \left. - \frac{1}{\beta^{(k-1)}} (\dot{\eta}^{(k)} - \dot{\eta}^{(k-1)}) \right\|_F \\
&\leq \lim_{k \rightarrow +\infty} \|(\lambda \dot{\mathbf{A}}^* \dot{\mathbf{A}} + \beta^{(k)} \dot{\mathbf{I}})^{-1} (\lambda \dot{\mathbf{A}}^* \dot{\mathbf{Y}} - \lambda \dot{\mathbf{A}}^* \dot{\mathbf{A}} \dot{\mathbf{Z}}^{(k)} - \dot{\eta}^{(k)})\|_F \\
&\quad + \frac{1}{\beta^{(k-1)}} \|\dot{\eta}^{(k)} - \dot{\eta}^{(k-1)}\|_F = 0.
\end{aligned} \tag{53}$$

Since $\dot{\mathbf{Z}}^{(k+1)} = \frac{1}{\beta^{(k)}} \dot{\eta}^{(k)} - \frac{1}{\beta^{(k)}} \dot{\eta}^{(k+1)} + \dot{\mathbf{X}}^{(k+1)}$, we conclude that

$$\begin{aligned}
\lim_{k \rightarrow +\infty} \|\dot{\mathbf{Z}}^{(k+1)} - \dot{\mathbf{Z}}^{(k)}\|_F &= \lim_{k \rightarrow +\infty} \left\| \frac{1}{\beta^{(k)}} \dot{\eta}^{(k)} - \frac{1}{\beta^{(k)}} \dot{\eta}^{(k+1)} + \dot{\mathbf{X}}^{(k+1)} - \dot{\mathbf{Z}}^{(k)} \right\|_F \\
&= \lim_{k \rightarrow +\infty} \left\| \dot{\mathbf{X}}^{(k)} + \frac{1}{\beta^{(k-1)}} \dot{\eta}^{(k-1)} - \dot{\mathbf{Z}}^{(k)} + \dot{\mathbf{X}}^{(k+1)} \right. \\
&\quad \left. - \dot{\mathbf{X}}^{(k)} - \frac{1}{\beta^{(k-1)}} \dot{\eta}^{(k-1)} + \frac{1}{\beta^{(k)}} \dot{\eta}^{(k)} - \frac{1}{\beta^{(k)}} \dot{\eta}^{(k+1)} \right\|_F \\
&\leq \lim_{k \rightarrow +\infty} \sum_{j=1}^N \left\| \sum_i Jw_{ij}^{(k-1)} / \beta^{(k-1)} \right\|_F + \|\dot{\mathbf{X}}^{(k+1)} - \dot{\mathbf{X}}^{(k)}\|_F \\
&\quad + \left\| \frac{1}{\beta^{(k-1)}} \dot{\eta}^{(k-1)} - \frac{1}{\beta^{(k)}} \dot{\eta}^{(k)} + \frac{1}{\beta^{(k)}} \dot{\eta}^{(k+1)} \right\|_F = 0.
\end{aligned} \tag{54}$$

This completes the proof. ■

It can be seen intuitively from Fig. 1 that $\|\dot{\mathbf{X}}^{(k+1)} - \dot{\mathbf{X}}^{(k)}\|_F$, $\|\dot{\mathbf{Z}}^{(k+1)} - \dot{\mathbf{Z}}^{(k)}\|_F$ and $\|\dot{\mathbf{X}}^{(k+1)} - \dot{\mathbf{Z}}^{(k+1)}\|_F$ simultaneously approach 0 during the iteration process.

4 Experimental Results

To demonstrate the effectiveness of our proposed QWSNM algorithm, we carry out extensive experiments on two representative CIR tasks, i.e., color image denoising and deblurring. To evaluate the quality of the restored images, the

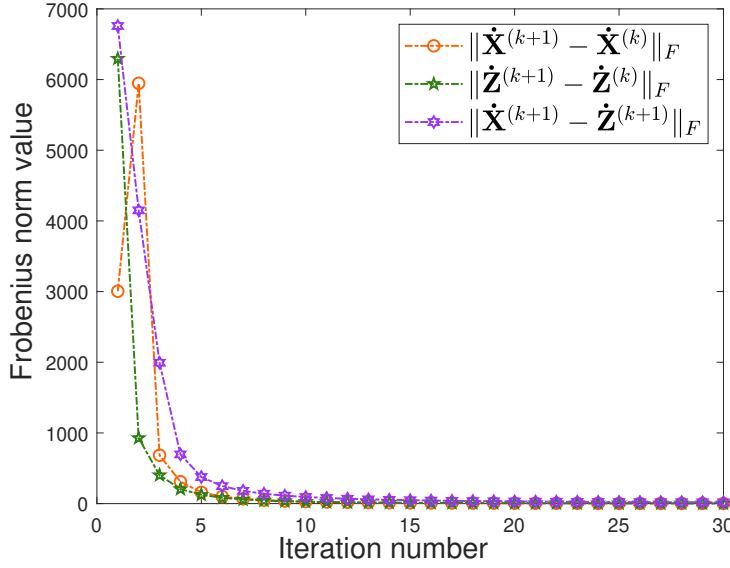


Fig. 1: The convergence curves of $\|\hat{\mathbf{X}}^{(k+1)} - \hat{\mathbf{X}}^{(k)}\|_F$, $\|\hat{\mathbf{Z}}^{(k+1)} - \hat{\mathbf{Z}}^{(k)}\|_F$ and $\|\hat{\mathbf{X}}^{(k+1)} - \hat{\mathbf{Z}}^{(k+1)}\|_F$ of the proposed QWSNM algorithm. Test image: “Bird”.



Fig. 2: Images in Set12 [57].

peak signal to noise ratio (PSNR) and structural similarity (SSIM) [56] are chosen as the quantitative metrics. Generally, a higher PSNR value suggests the recovery result is of higher quality, but in some scenarios it may not. To this end, the perceptual quality metric SSIM [56] is calculated to evaluate the visual quality. The higher SSIM value indicates the better visual quality. All the experiments were implemented in Matlab 2021b on a desktop with 3.30GHz CPU and 16GB RAM.

Methods	SV-TV [58]	CBM3D [29]	IRCNN [59]	pQSTV [60]	QWNNM [36]	QWSNM (Ours)
$\sigma = 15$						
Bird	31.16/0.9383	32.54/0.9567	32.96/0.9607	31.17/0.9414	32.77/0.9565	32.86/0.9593
Plane	30.82/0.8940	33.76/0.9554	34.25/0.9573	32.72/0.9382	<u>34.69/0.9598</u>	34.81/0.9607
Baboon	28.14/0.9321	29.59/0.9474	29.96/0.9514	28.68/0.9344	<u>30.18/0.9537</u>	30.24/0.9539
Bee	31.09/0.9394	34.69/0.9647	35.31/0.9696	34.06/0.9606	<u>35.78/0.9729</u>	35.81/0.9733
Aquatic	31.19/0.9093	33.31/0.9491	33.82/0.9517	31.96/0.9335	<u>33.88/0.9532</u>	34.06/0.9537
Barbara	29.64/0.9349	32.67/0.9641	32.57/0.9603	31.57/0.9526	<u>33.14/0.9662</u>	33.24/0.9672
Boat	30.38/0.9132	32.71/0.9631	33.30/0.9672	31.47/0.9501	<u>33.08/0.9659</u>	33.15/0.9661
House	30.82/0.9575	34.85/0.9801	34.07/0.9779	33.42/0.9746	<u>34.74/0.9796</u>	<u>34.72/0.9794</u>
Peppers	28.82/0.9750	32.53/0.9888	32.85/0.9899	32.18/0.9881	<u>33.35/0.9907</u>	33.42/0.9908
Starfish	31.00/0.9718	32.96/0.9862	33.61/0.9879	31.79/0.9822	<u>33.38/0.9866</u>	33.43/0.9869
Lena	32.15/0.9843	33.94/0.9892	33.91/0.9891	33.00/0.9866	<u>34.13/0.9898</u>	34.15/0.9899
Pelican	31.15/0.9084	32.65/0.9449	32.37/0.9376	31.26/0.9218	<u>32.88/0.9479</u>	32.94/0.9489
Average	30.53/0.9382	33.02/0.9658	33.25/0.9667	31.94/0.9553	<u>33.50/0.9686</u>	33.57/0.9692
$\sigma = 25$						
Bird	28.23/0.8875	29.73/0.9225	30.22/0.9311	28.39/0.8973	29.52/0.9223	30.11/0.9291
Plane	28.95/0.8586	31.14/0.8586	31.63/0.9346	30.06/0.9055	<u>32.10/0.9415</u>	32.16/0.9425
Baboon	25.46/0.8650	27.05/0.9032	27.44/0.9132	26.19/0.8827	<u>27.62/0.9145</u>	27.66/0.9166
Bee	29.73/0.9219	32.48/0.9483	32.98/0.9537	31.90/0.9417	<u>33.30/0.9563</u>	33.38/0.9569
Aquatic	28.80/0.8716	30.68/0.9215	31.23/0.9275	29.39/0.8992	<u>31.27/0.9290</u>	31.30/0.9301
Barbara	27.39/0.9006	30.04/0.9390	30.10/0.9376	28.89/0.9212	<u>30.49/0.9445</u>	30.59/0.9455
Boat	28.06/0.8949	29.92/0.9372	30.59/0.9458	28.70/0.9181	<u>30.31/0.9437</u>	30.39/0.9443
House	29.15/0.9479	33.03/0.9721	32.13/0.9694	31.78/0.9649	<u>32.93/0.9717</u>	33.01/0.9719
Peppers	27.09/0.9655	30.06/0.9812	30.46/0.9832	29.51/0.9794	<u>30.84/0.9841</u>	30.92/0.9844
Starfish	28.90/0.9666	30.27/0.9770	30.99/0.9800	28.99/0.9705	<u>30.89/0.9786</u>	30.90/0.9787
Lena	29.78/0.9738	32.27/0.9847	32.30/0.9849	31.42/0.9814	<u>32.49/0.9856</u>	32.55/0.9858
Pelican	27.77/0.8491	30.51/0.9206	30.58/0.9186	29.48/0.8976	<u>30.74/0.9226</u>	30.76/0.9237
Average	28.28/0.9086	30.60/0.9449	30.86/0.9483	29.56/0.9300	<u>31.04/0.9485</u>	31.14/0.9508
$\sigma = 35$						
Bird	26.55/0.8869	27.92/0.8869	28.53/0.9022	26.91/0.8574	28.32/0.8974	28.40/0.8996
Plane	27.36/0.7858	29.34/0.9055	29.89/0.9113	28.41/0.8734	<u>30.32/0.9233</u>	30.41/0.9253
Baboon	24.38/0.8278	25.40/0.8555	25.94/0.8718	24.71/0.8329	<u>26.00/0.8726</u>	26.10/0.8779
Bee	28.31/0.8914	30.86/0.9333	31.50/0.9405	30.56/0.9268	<u>31.82/0.9433</u>	31.92/0.9439
Aquatic	27.05/0.8099	28.81/0.8890	29.47/0.9024	27.56/0.8563	<u>29.48/0.9041</u>	29.62/0.9075
Barbara	26.01/0.8682	28.15/0.9120	28.57/0.9179	27.30/0.8937	<u>28.77/0.9219</u>	28.89/0.9237
Boat	26.45/0.8472	28.00/0.9083	28.86/0.9238	27.19/0.8904	<u>28.48/0.9183</u>	28.57/0.9194
House	27.75/0.9283	31.58/0.9636	30.78/0.9617	30.53/0.9564	<u>31.88/0.9659</u>	32.06/0.9668
Peppers	26.04/0.9562	28.19/0.9722	28.88/0.9764	28.02/0.9712	<u>29.21/0.9774</u>	29.30/0.9780
Starfish	27.19/0.9485	28.38/0.9672	29.36/0.9725	27.50/0.9602	<u>29.23/0.9713</u>	29.25/0.9715
Lena	28.60/0.9665	30.91/0.9799	31.16/0.9812	30.22/0.9764	<u>31.30/0.9818</u>	31.38/0.9821
Pelican	26.62/0.8042	29.09/0.8994	29.34/0.9011	28.56/0.8743	<u>29.36/0.9039</u>	29.41/0.9066
Average	26.86/0.8729	28.89/0.9227	29.35/0.9307	28.12/0.9059	<u>29.52/0.9318</u>	29.61/0.9335
$\sigma = 45$						
Bird	25.19/0.7892	26.87/0.8602	27.33/0.8743	25.84/0.8179	26.90/0.8594	<u>27.13/0.8684</u>
Plane	26.16/0.8385	28.32/0.8887	28.72/0.8920	27.24/0.8496	29.00/0.9040	29.11/0.9086
Baboon	23.38/0.7797	24.43/0.8150	24.91/0.8431	23.81/0.7951	24.75/0.8278	25.10/0.8512
Bee	27.39/0.8721	30.06/0.9237	<u>30.43/0.9293</u>	29.44/0.9122	30.73/0.9309	30.83/0.9338
Aquatic	25.74/0.7645	27.73/0.8656	<u>28.21/0.8780</u>	26.29/0.8249	28.01/0.8745	28.27/0.8833
Barbara	24.81/0.8349	27.25/0.8658	<u>27.49/0.9015</u>	26.01/0.8689	27.45/0.8988	27.55/0.9035
Boat	25.08/0.8060	26.79/0.8851	27.62/0.9029	25.81/0.8612	26.98/0.8866	<u>27.23/0.8942</u>
House	26.79/0.9120	30.86/0.9584	29.95/0.9547	29.46/0.9455	31.31/0.9620	<u>31.29/0.9619</u>
Peppers	25.19/0.9474	27.02/0.9647	27.74/0.9699	26.83/0.9634	28.01/0.9713	<u>27.97/0.9710</u>
Starfish	25.85/0.9339	27.36/0.9612	28.04/0.9657	26.30/0.9495	28.01/0.9625	<u>28.02/0.9638</u>
Lena	27.37/0.9568	30.26/0.9772	30.29/0.9778	29.21/0.9714	30.18/0.9773	30.37/0.9783
Pelican	25.33/0.7549	28.25/0.8876	<u>28.44/0.8889</u>	27.23/0.8505	28.28/0.8824	28.45/0.8908
Average	25.69/0.8492	27.93/0.9044	<u>28.26/0.9147</u>	26.96/0.8842	<u>28.30/0.9115</u>	28.44/0.9174

Table 2: Comparison of the denoising PSNR (dB) values. The best results are highlighted in **bold** and the second-best results are underlined.

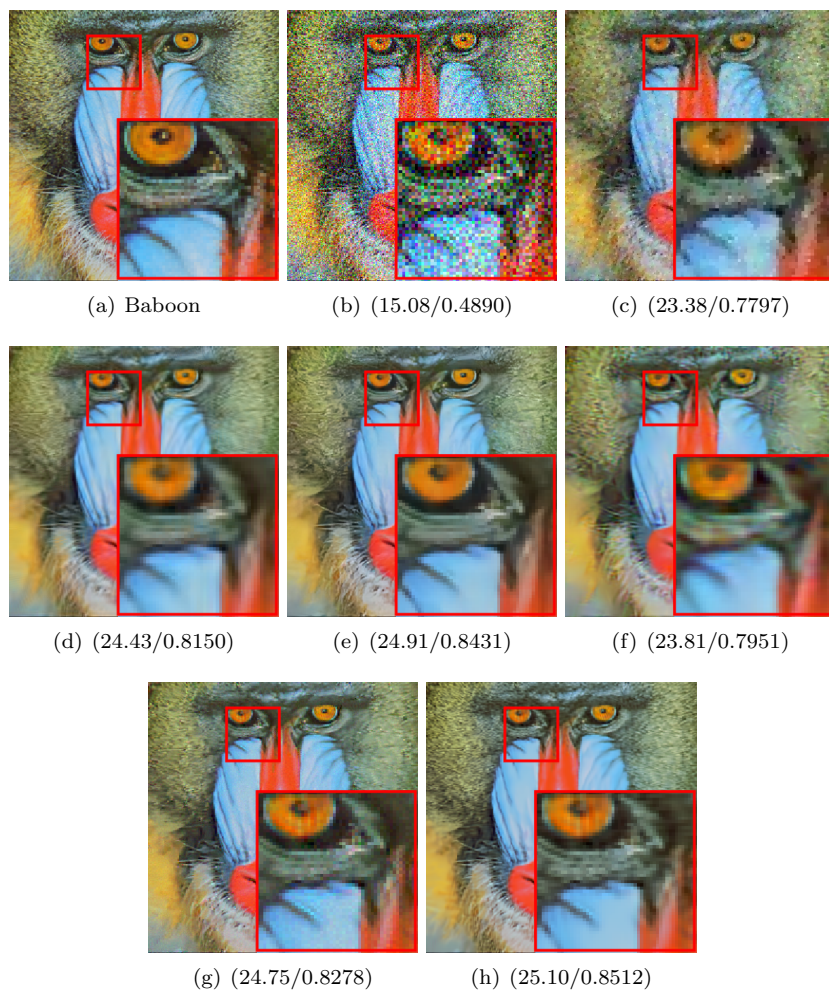


Fig. 3: Denoising performance on “Baboon” with visual quality and numerical results (PSNR/SSIM). (a) Ground truth; (b) Noisy image ($\sigma = 45$); (c) SV-TV [58]; (d) CBM3D [29]; (e) IRCNN [59]; (f) pQSTV [60]; (g) QWNNM [36]; (h) QWSNM (Ours).

4.1 Color Image Denoising

For the color image denoising, the recovery performance is evaluated on the benchmark Set12³ dataset, which contains 12 natural RGB color images shown

³ The test images of Set12 are mainly collected from Wang et al. [57]. Concretely, Bird, Plane, Baboon, Bee, Aquatic, Barbara, Boat, House, Peppers and Starfish are all with the size of 256×256 , Lena and Pelican are with the size of 512×512 .

in Fig. 2. All the color noisy images are synthesized by adding the Gaussian noise with mean zero and variance σ^2 . To be concrete, we test the scenarios of noise levels σ equal to 15, 25, 35 and 45 respectively. In our experiments, we compare our proposed QWSNM algorithm with several prevailing methods, including SV-TV [58], CBM3D [29], IRCNN [59], QWNNM [36], pQSTV [60]. Particularly, it is noted that SV-TV, QWNNM and pQSTV are all quaternion-based methods which represent the color image via a pure quaternion matrix to preserve the relationship of three channels. IRCNN [59] is a convolution neural network method which was trained to handle a wide range of noise levels. CBM3D [29] applies the classical BM3D algorithm to the denoising of color images and its working principle is to convert the color image from the RGB space into a less correlated luminance-chrominance space. For the comparison methods, the involved parameters are all manually-tuned or automatically set up according to the reference papers to achieve the best performance. In our proposed algorithm, parameters that need to be considered include the patch size w , similar patch number M , search window W , the power p value in the weighted Schatten p norm regularizer, the iteration number K , the parameters c and ϵ in the weight $w_i = \frac{c}{\sigma_i(\mathbf{X}) + \epsilon}$. For $\sigma \leq 40$, we set the search window W as 30. When $0 < \sigma \leq 20$, we set the similar patch number M , the patch size $w \times w$ and the iteration number K as 70, 4×4 , and 8, respectively. When $20 < \sigma \leq 40$, we set the similar number M , the patch size $w \times w$ and the iteration number K as 90, 5×5 , and 12, respectively. For $40 < \sigma \leq 50$, we set the search window W , the similar patch number M , the patch size $w \times w$ and the iteration number K as 40, 120, 5×5 , and 14, respectively. Throughout the denoising experiments, we fix the power p value and the regularization parameter λ as 0.95 and 1 for simplicity. In addition, the parameters c and ϵ are set as $\sqrt{2}$ and `eps` (a Matlab built-in function) respectively, which is as the same as the parameter setting in the WNNM [23].

Table 2 reports the PSNR and SSIM values of each image as well as the average results of the competing approaches under different noise levels. The best results are highlighted in bold and the second-best results are underlined. One can observe that our proposed QWSNM algorithm achieves the best objective performance in most cases. For the PSNR metric, our method achieves 0.32dB, 0.28dB, 0.26dB and 0.18dB improvement over the state-of-the-art approach IRCNN [59] on average with respect to $\sigma = 15, 25, 35, 45$. The main

reason behind this phenomenon is that we adopt the quaternion representation, which can better preserve the inter-relationship between RGB channels. Compared with the most similar quaternion-based approach QWNNM [36], our method achieves slight quantitative gain of 0.07dB, 0.10dB, 0.09dB and 0.14dB on average with respect to $\sigma = 15, 25, 35, 45$. A reasonable explanation is that QWNNM [36] tends to over-shrink the dominant rank components, which constraints its capacity of recovering the images with rich textures. The above quantitative results fully demonstrate the effectiveness of exploiting both the quaternion representation and WSNM regularization jointly, as in our proposed QWSNM approach. Human subject perception is the ultimate judge of image quality, which also plays a crucial role in the estimation of denoising algorithms. The visual quality comparisons for the test image “Baboon” are shown in Fig. 3. As can be observed from the highlighted window, SV-TV method produces agonizing visual artifacts, while CBM3D, IRCNN and pQSTV approaches are prone to over-smooth the image, losing some of the tiny details. Although QWNNM method overcomes the over-smooth phenomenon, it generates unpleasant visual artifacts. In contrast, our proposed QWSNM approach is not only capable of achieving a better visual perception of both texture and detail information, but also significantly eliminating visual artifacts.

4.2 Color Image Deblurring

In this subsection, we conduct extensive color image deblurring experiments to demonstrate the superiority of our proposed QWSNM. The test images are selected from Set12 and Set27⁴, which are shown in Figs. 2 and 4, respectively. Three sets of experiments are conducted for simulated color image deblurring. The first is a 9×9 uniform kernel, the second is a Gaussian kernel with standard variation 1.6, and the third is a motion kernel with motion length 20 and motion angle 60. Then, additive Gaussian noise with $\sigma = 15$ is added to the

⁴ The test images of Set27 are downloaded from <https://github.com/Huang-chao-yan/dataset>. Image 1-7 and 16 are with the size of 500×500 ; Image 8 is with the size of 560×392 ; Image 9 and 22-25 are with the size of 481×321 ; Image 10 and 21 are with the size of 1024×683 ; Image 11 is with the size of 1024×764 ; Image 12 is with the size of 321×481 ; Image 13 is with the size of 1024×701 ; Image 14 is with the size of 1024×783 ; Image 15 is with the size of 1024×684 ; Image 17 is with the size of 1024×605 ; Image 18 is with the size of 448×296 ; Image 19 is with the size of 256×256 ; Image 20 is with the size of 288×288 ; Image 26 is with the size of 418×378 ; Image 27 is with the size of 1024×937 .

blurred images. The involved parameters of our algorithm are set as follows: $\lambda = 65$, $\beta = 7.5$ for Gaussian blur with noise; $\lambda = 115$, $\beta = 7.5$ for motion blur with noise; $\lambda = 115$, $\beta = 8.5$ for average blur with noise. Particularly, we fix the search window size W , the similar number M and the patch size w as 30, 155 and 6×6 , respectively. Moreover, we study the influence of the parameters c and ϵ in the weight $w_i = \frac{c}{\sigma_i(\mathbf{X}) + \epsilon}$. Experiments on the test image ‘‘Bird’’ with motion blur and noise are conducted, where c is set to $[0.1 : 5] * \sqrt{2}$ with an increment of 0.2 and ϵ is set to $[1, 250000] * \mathbf{eps}$ with step size 10000. As shown in Fig. 4, the parameter ϵ does not dramatically affect the results and we set $\epsilon = \mathbf{eps}$ for all our deblurring experiments. The adjustment of parameter c has a greater impact on the results and we set $c = 2.2 * \sqrt{2}$ for all deblurring experiments through trial and error.

We compare the proposed QWSNM with five representative methods including SV-TV [58], IDD-BM3D [9], IRCNN [59], MSWNNM [61] and QWNNM* [37]. The PSNR and SSIM values of compared deblurring methods with average blur AB(9,9)/ $\sigma = 15$ are shown in Table 3. The corresponding results with motion blur MB(20,60)/ $\sigma = 15$ and with Gaussian blur GB(25,1.6)/ $\sigma = 15$ are reported in Tables 4 and 5, respectively. The best results are highlighted in bold and the second-best results are underlined. As expected, it can be observed that the proposed QWSNM approach consistently generates much better deblurring results on average on different types of blur. Moreover, we display the restored images to demonstrate the perceptual superiority of the proposed method. Figs. 6, 7, 8 show the visual results of these competing methods. For Img26, we can clearly observe that SV-TV, IDD-BM3D, IRCNN and MSWNNM are apt to over-smooth the text image, leading to the characters unrecognizable. Although QWNNM approach achieves better visual results than the above four methods, it still tends to generate the over-smooth phenomenon. By contrast, the text image recovered by our proposed QWSNM is sharper and the characters can be better recognized. For Img1, it is evident that SV-TV method generates color distortions and color artifacts, while IDD-BM3D, IRCNN and MSWNNM approaches are prone to over-smooth the image, losing many vital details. Although QWNNM method can prevent the over-smooth phenomenon to some extent, benefiting from the advantages of quaternion representation, it is still not able to recover some of the texture structures. Compared with these competing methods, our proposed QWSNM achieves

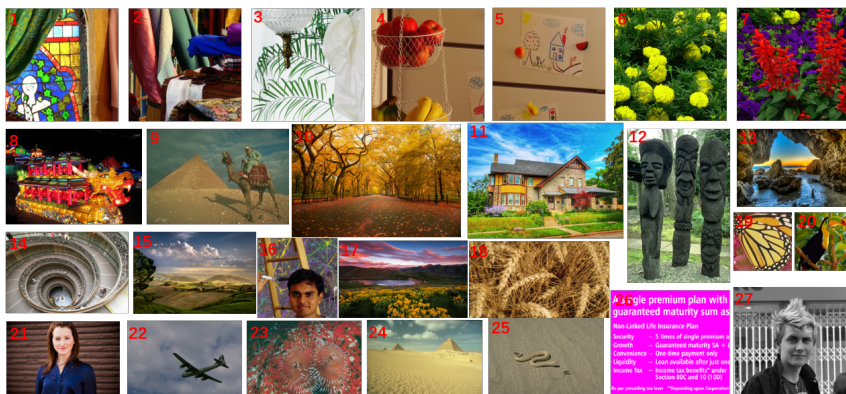


Fig. 4: Images in Set27 [37].

the best visual results on the whole, which not only preserves more texture structures in the wallpaper of the window, but also effectively eliminates the undesirable color distortions.

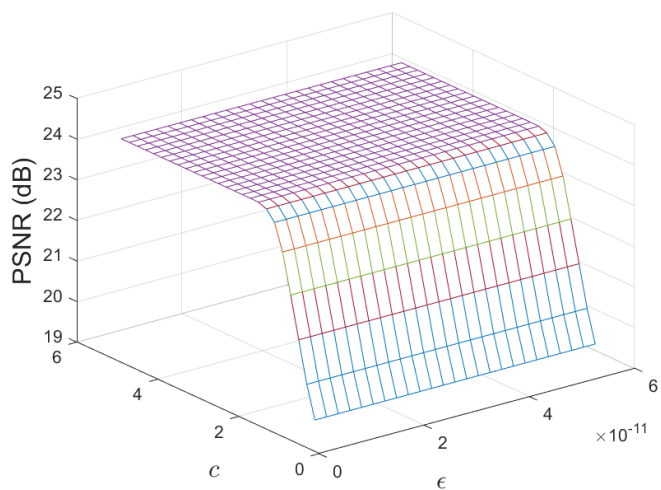


Fig. 5: Evolution of PSNR values with different parameters c and ϵ in the case of motion deblurring. Test image: “Bird”.

Methods	SV-TV [58]	IDD-BM3D [9]	IRCNN [59]	MSWNNM [61]	QWNNM* [37]	QWSNM (Ours)
Set27						
Img1	21.50/0.8369	21.47/0.8348	22.68/0.8683	22.66/0.8672	22.83/0.8696	23.17/0.8764
Img2	25.59/0.8497	25.02/0.8460	26.53/0.8714	26.52/0.8712	26.45/0.8712	26.64/0.8724
Img3	21.85/0.7563	20.92/0.7365	23.52/0.8177	23.60/0.8221	23.95/0.8189	24.41/0.8350
Img4	26.31/0.9564	26.07/0.9546	27.42/0.9653	27.45/0.9657	27.68/0.9671	27.81/0.9680
Img5	29.92/0.9710	29.89/0.9716	31.58/0.9806	31.68/0.9808	31.85/0.9815	32.01/0.9823
Img6	23.00/0.8640	22.92/0.8619	23.78/0.8791	23.73/0.8792	24.07/0.8865	24.14/0.8870
Img7	23.76/0.8541	24.36/0.8699	24.99/0.8845	24.93/0.8839	25.25/0.8914	25.34/0.8931
Img8	21.03/0.7982	21.25/0.8430	22.18/0.8658	22.13/0.8398	22.53/0.8686	22.81/0.8694
Img9	28.71/0.9310	28.61/0.9343	28.92/0.9385	28.91/0.9384	28.98/0.9391	29.00/0.9394
Img10	19.65/0.8445	19.59/0.8439	20.30/0.8648	20.26/0.8639	20.57/0.8723	20.63/0.8743
Img11	20.75/0.8124	20.59/0.8071	21.63/0.8414	21.58/0.8386	21.96/0.8502	22.06/0.8536
Img12	21.77/0.5826	21.16/0.5424	21.89/0.5992	21.83/0.5919	21.88/0.5960	21.92/0.5995
Img13	23.59/0.7909	23.27/0.7856	24.43/0.8228	24.38/0.8169	24.65/0.8267	24.71/0.8324
Img14	22.53/0.7253	22.09/0.7085	23.66/0.7786	23.68/0.7807	24.02/0.7885	24.30/0.7978
Img15	27.86/0.9044	27.54/0.9051	28.60/0.9152	28.58/0.9150	28.72/0.9173	28.74/0.9176
Img16	26.01/0.8077	26.58/0.8237	27.46/0.8419	27.46/0.8402	28.08/0.8604	28.18/0.8606
Img17	23.36/0.8375	23.36/0.8375	24.15/0.8592	24.11/0.8573	24.37/0.8589	24.47/0.8621
Img18	18.97/0.8045	18.78/0.7964	19.21/0.8166	19.15/0.8136	19.42/0.8246	19.48/0.8256
Img19	22.06/0.8944	20.87/0.8584	22.60/0.9038	22.72/0.9065	23.05/0.9069	23.43/0.9191
Img20	26.07/0.9135	26.63/0.9347	27.83/0.9446	27.88/0.9452	27.71/0.9431	27.94/0.9475
Img21	32.12/0.9536	32.52/0.9663	33.71/0.9677	33.73/0.9700	33.24/0.9651	33.30/0.9656
Img22	33.60/0.9458	32.61/0.9524	34.06/0.9607	34.26/0.9619	33.78/0.9526	34.04/0.9544
Img23	23.43/0.8129	23.28/0.8104	23.88/0.8333	23.80/0.8292	24.26/0.8466	24.30/0.8482
Img24	29.27/0.9563	29.14/0.9590	29.69/0.9645	29.65/0.9642	29.55/0.9619	29.64/0.9627
Img25	26.00/0.7769	25.83/0.7733	26.17/0.7843	26.13/0.7810	26.13/0.7807	26.15/0.7814
Img26	17.23/0.9039	18.23/0.9241	19.31/0.9480	19.03/0.9380	20.48/0.9544	21.06/0.9610
Img27	29.13/0.8344	29.12/0.8608	31.14/0.8848	31.10/0.8835	30.67/0.8739	30.84/0.8744
Average	24.63/0.8487	24.51/0.8490	25.60/0.8743	25.59/0.8684	25.76/0.8762	25.94/0.8799
Set12						
Bird	23.01/0.7037	22.77/0.6913	23.33/0.7240	23.27/0.7191	23.49/0.7316	23.55/0.7361
Plane	24.24/0.7709	23.80/0.7837	25.00/0.8220	24.98/0.8222	25.12/0.8265	25.22/0.8295
Baboon	22.02/0.6954	21.97/0.6790	22.38/0.7004	22.31/0.6945	22.37/0.6984	22.46/0.7023
Bee	27.03/0.8886	28.11/0.9103	28.67/0.9129	28.75/0.9137	29.09/0.9174	29.20/0.9186
Aquatic	23.26/0.7307	22.89/0.7308	24.06/0.7804	24.03/0.7824	24.11/0.7861	24.28/0.7874
Barbara	22.86/0.7804	22.66/0.7731	23.60/0.8070	23.60/0.8068	23.62/0.8040	23.79/0.8087
Boat	22.38/0.7679	21.71/0.7555	22.98/0.8019	22.93/0.7977	22.96/0.8006	23.17/0.8042
House	26.34/0.9085	26.64/0.9111	28.04/0.9335	28.15/0.9342	28.61/0.9360	28.95/0.9395
Peppers	22.57/0.9251	23.73/0.9298	24.63/0.9413	24.65/0.9415	24.64/0.9405	24.80/0.9440
Starfish	23.15/0.9207	23.02/0.9251	23.86/0.9354	23.83/0.9354	24.03/0.9365	24.15/0.9367
Lena	27.55/0.9575	27.29/0.9560	28.41/0.9643	28.39/0.9639	28.37/0.9640	28.60/0.9654
Pelican	24.58/0.8221	23.93/0.8122	24.85/0.8402	24.75/0.8394	24.92/0.8339	25.04/0.8362
Average	24.08/0.8226	24.04/0.8215	24.98/0.8469	24.97/0.8459	25.11/0.8471	25.27/0.8507

Table 3: PSNR (dB) and SSIM values of different restoration models for AB(9,9)/ $\sigma = 15$. The best results are highlighted in **bold** and the second-best results are underlined.

Methods	SV-TV [58]	IDD-BM3D [9]	IRCNN [59]	MSWNNM [61]	QWNNM* [37]	QWSNM (Ours)
Set27						
Img1	23.28/0.8822	23.46/0.8822	24.20/0.9052	24.19/0.9056	24.46/0.9075	24.50/0.9089
Img2	27.16/0.8803	27.02/0.8871	28.19/0.8988	28.30/0.9032	28.32/0.9041	28.38/0.9063
Img3	25.12/0.8501	24.53/0.8442	<u>26.84/0.8804</u>	26.78/0.8667	<u>26.80/0.8930</u>	27.15/0.8950
Img4	27.99/0.9690	28.20/0.9702	29.34/0.9764	<u>29.74/0.9787</u>	29.68/0.9785	29.79/0.9791
Img5	31.61/0.9796	32.58/0.9841	33.18/0.9861	33.52/0.9870	33.90/0.9879	33.96/0.9881
Img6	25.03/0.9077	25.00/0.9047	26.17/0.9228	26.18/0.9248	<u>26.24/0.9250</u>	26.31/0.9261
Img7	26.04/0.9074	26.73/0.9171	27.57/0.9303	27.52/0.9311	<u>27.71/0.9339</u>	27.76/0.9350
Img8	22.71/0.8209	23.26/0.8923	23.94/0.8764	23.93/0.7691	<u>24.27/0.8975</u>	24.37/0.8992
Img9	29.57/0.9378	29.50/0.9455	29.69/0.9441	29.77/0.9452	<u>29.90/0.9493</u>	29.96/0.9500
Img10	20.64/0.8724	20.70/0.8749	21.58/0.8963	21.57/0.8960	<u>21.72/0.8998</u>	21.77/0.9013
Img11	21.78/0.8459	21.79/0.8423	22.77/0.8746	22.78/0.8741	<u>22.94/0.8750</u>	23.00/0.8773
Img12	22.81/0.6606	22.12/0.6088	22.95/0.6760	22.93/0.6698	22.85/0.6606	22.90/0.6653
Img13	25.39/0.8491	24.90/0.8347	26.40/0.8760	<u>26.35/0.8750</u>	26.52/0.8776	26.56/0.8786
Img14	24.69/0.8160	24.19/0.7977	25.89/0.8449	25.83/0.8432	<u>26.14/0.8604</u>	26.25/0.8619
Img15	29.25/0.9241	29.01/0.9225	29.85/0.9293	29.80/0.9279	<u>30.13/0.9373</u>	30.19/0.9378
Img16	28.16/0.8641	29.37/0.8897	30.12/0.8979	30.10/0.8965	<u>30.76/0.9108</u>	30.80/0.9114
Img17	24.51/0.8674	24.67/0.8682	25.45/0.8806	25.40/0.8785	<u>25.64/0.8869</u>	25.67/0.8875
Img18	20.44/0.8585	20.28/0.8523	20.90/0.8747	20.86/0.8722	<u>21.01/0.8776</u>	21.06/0.8791
Img19	24.85/0.9386	23.93/0.9248	25.70/0.9494	25.69/0.9489	25.27/0.9444	25.44/0.9459
Img20	28.10/0.9310	29.60/0.9626	30.58/0.9597	<u>30.56/0.9588</u>	30.84/0.9676	30.87/0.9688
Img21	33.50/0.9624	34.15/0.9743	34.37/0.9684	34.35/0.9678	35.01/0.9757	<u>34.90/0.9743</u>
Img22	34.47/0.9306	34.81/0.9658	35.33/0.9439	35.45/0.9500	35.84/0.9635	<u>35.76/0.9600</u>
Img23	25.55/0.8834	25.44/0.8784	26.30/0.9022	26.38/0.9025	26.60/0.9065	26.62/0.9071
Img24	30.06/0.9603	29.85/0.9655	30.41/0.9667	30.45/0.9672	<u>30.51/0.9698</u>	30.54/0.9701
Img25	26.42/0.7889	26.25/0.7826	26.50/0.7918	26.39/0.7912	<u>26.48/0.7916</u>	26.52/0.7920
Img26	19.56/0.9405	21.99/0.9689	22.84/0.9740	22.69/0.9658	23.35/0.9777	23.60/0.9791
Img27	31.18/0.8735	31.12/0.8925	32.77/0.8883	32.70/0.8856	<u>32.89/0.9084</u>	32.96/0.9098
Average	26.29/0.8853	26.46/0.8903	27.40/0.9044	27.43/0.9007	<u>27.62/0.9099</u>	27.69/0.9109
Set12						
Bird	24.52/0.7808	24.47/0.7736	25.12/0.8080	25.14/0.8084	25.20/0.8093	25.27/0.8130
Plane	25.90/0.8014	26.04/0.8527	27.04/0.8561	27.18/0.8744	<u>27.19/0.8776</u>	27.30/0.8895
Baboon	22.97/0.7466	22.98/0.7282	23.42/ 0.7617	23.36/0.7533	<u>23.43/0.7516</u>	23.48/0.7572
Bee	28.66/0.9039	30.26/0.9308	30.65/0.9293	30.98/0.9363	31.32/0.9391	31.42/0.9455
Aquatic	25.09/0.7961	25.37/0.8271	26.30/0.8486	26.42/0.8638	<u>26.51/0.8669</u>	26.58/0.8702
Barbara	24.15/0.8275	24.27/0.8301	24.91/0.8530	<u>24.94/0.8543</u>	24.92/0.8517	25.00/0.8585
Boat	23.68/0.8086	23.62/0.8365	<u>24.71/0.8501</u>	24.74/0.8534	24.55/0.8504	24.62/0.8585
House	27.32/0.9242	28.61/0.9402	29.10/0.9456	29.12/0.9460	<u>29.82/0.9496</u>	29.90/0.9500
Peppers	25.55/0.9501	25.94/0.9561	<u>26.65/0.9622</u>	26.64/0.9620	<u>26.57/0.9615</u>	26.69/0.9643
Starfish	25.15/0.9388	25.47/0.9487	<u>26.60/0.9557</u>	26.65/0.9560	26.67/0.9596	26.77/0.9654
Lena	29.06/0.9684	29.27/0.9691	30.27/0.9754	30.24/0.9750	<u>30.48/0.9761</u>	30.55/0.9800
Pelican	25.70/0.8403	25.15/0.8412	<u>26.18/0.8610</u>	26.16/0.8605	26.13/0.8602	26.26/0.8701
Average	25.65/0.8572	25.95/0.8687	<u>26.75/0.8839</u>	26.80/0.8870	<u>26.90/0.8878</u>	26.98/0.8931

Table 4: PSNR (dB) and SSIM values of different restoration models for GB(25,1.6)/ $\sigma = 15$. The best results are highlighted in **bold** and the second-best results are underlined.

Methods	SV-TV [58]	IDD-BM3D [9]	IRCNN [59]	MSWNNM [61]	QWNNM* [37]	QWSNM (Ours)
Set27						
Img1	20.89/0.8342	20.66/0.8272	22.58/0.8764	22.56/0.8752	22.55/0.8728	22.92/0.8810
Img2	24.96/0.8331	24.20/0.8279	26.13/0.8668	26.13/0.8660	26.19/0.8695	26.35/0.8715
Img3	22.05/0.7712	20.01/0.7163	24.05/0.8387	24.14/0.8399	24.06/0.8359	24.24/0.8412
Img4	26.47/0.9591	26.03/0.9561	27.77/0.9684	27.80/0.9687	28.22/0.9712	28.28/0.9714
Img5	29.47/0.9695	29.13/0.9691	31.08/0.9788	31.11/0.9787	31.68/0.9816	31.83/0.9820
Img6	22.59/0.8520	22.29/0.8458	23.62/0.8755	23.57/0.8741	23.88/0.8815	23.99/0.8833
Img7	22.50/0.8231	23.05/0.8408	24.23/0.8703	24.16/0.8690	24.56/0.8799	24.71/0.8834
Img8	20.40/0.7541	20.80/0.8098	21.79/0.8535	21.74/0.7293	22.17/0.9099	22.48/0.9352
Img9	28.14/0.9202	27.93/0.9251	28.61/0.9360	28.55/0.9350	28.58/0.9349	28.59/0.9351
Img10	19.48/0.8410	19.23/0.8370	20.29/0.8647	20.24/0.8632	20.58/0.8728	20.65/0.8748
Img11	20.30/0.8028	19.92/0.7916	21.33/0.8362	21.27/0.8330	21.56/0.8435	21.76/0.8470
Img12	21.62/0.5859	20.84/0.5268	21.83/0.6056	21.75/0.5968	21.72/0.5975	21.82/0.5984
Img13	23.27/0.7840	22.56/0.7680	24.35/0.8222	24.27/0.8160	24.42/0.8224	24.59/0.8260
Img14	22.04/0.7166	21.15/0.6841	23.49/0.7790	23.49/0.7782	23.79/0.7840	24.13/0.7979
Img15	27.07/0.8937	26.36/0.8883	27.98/0.9097	27.93/0.9092	28.04/0.9070	28.19/0.9160
Img16	25.57/0.7891	25.71/0.8053	27.01/0.8327	27.01/0.8300	27.19/0.8436	27.66/0.8533
Img17	22.81/0.8187	22.58/0.8149	23.92/0.8478	23.88/0.8449	24.15/0.8467	24.32/0.8515
Img18	19.29/0.8263	18.87/0.8119	19.63/0.8408	19.56/0.8375	19.90/0.8507	19.96/0.8521
Img19	20.99/0.8738	19.19/0.8249	22.24/0.9006	22.33/0.9021	22.06/0.8943	22.27/0.8995
Img20	24.82/0.8786	25.09/0.9105	26.94/0.9377	26.94/0.9378	26.75/0.9357	27.03/0.9394
Img21	31.52/0.9483	31.60/0.9591	33.34/0.9670	33.35/0.9672	32.67/0.9611	32.75/0.9613
Img22	32.56/0.9247	30.88/0.9362	33.38/0.9594	33.47/0.9580	33.75/0.9549	33.81/0.9556
Img23	23.21/0.8145	22.88/0.8051	23.72/0.8366	23.64/0.8314	24.26/0.8542	24.32/0.8549
Img24	28.70/0.9483	28.57/0.9526	29.31/0.9604	29.24/0.9601	29.16/0.9578	29.17/0.9582
Img25	25.84/0.7787	25.63/0.7715	26.16/0.7884	26.07/0.7820	26.05/0.7831	26.08/0.7835
Img26	17.26/0.9082	18.42/0.9311	19.92/0.9496	19.68/0.9487	22.02/0.9705	22.08/0.9708
Img27	28.35/0.8276	27.05/0.8296	30.54/0.8824	30.50/0.8810	30.02/0.8649	30.32/0.8700
Average	24.15/0.8399	23.73/0.8358	25.38/0.8735	25.35/0.8685	25.56/0.8753	25.72/0.8813
Set12						
Bird	22.77/0.6867	22.37/0.6725	23.34/0.7266	23.25/0.7186	23.59/0.7417	23.62/0.7425
Plane	23.60/0.7149	23.16/0.7555	24.67/0.8134	24.66/0.8123	24.75/0.8196	24.83/0.8212
Baboon	21.70/0.6936	21.74/0.6730	22.16/0.7003	22.08/0.6912	22.26/0.7018	22.30/0.7024
Bee	25.48/0.8554	26.59/0.8868	27.97/0.9064	28.02/0.9066	28.63/0.9130	28.75/0.9140
Aquatic	22.77/0.6857	22.25/0.6919	23.91/0.7730	23.87/0.7732	24.16/0.7792	24.25/0.7835
Barbara	22.59/0.7728	22.44/0.7701	23.44/0.8113	23.40/0.8080	23.64/0.8168	23.74/0.8199
Boat	22.02/0.7383	21.11/0.7355	23.00/0.8068	22.93/0.8032	22.95/0.8043	23.03/0.8072
House	25.04/0.8795	25.02/0.8845	26.33/0.9132	26.46/0.9145	27.82/0.9275	28.00/0.9300
Peppers	23.15/0.9174	23.31/0.9257	24.56/0.9410	24.54/0.9405	24.42/0.9381	24.61/0.9412
Starfish	22.55/0.9069	22.15/0.9133	23.51/0.9339	23.47/0.9337	23.87/0.9368	23.95/0.9381
Lena	27.55/0.9564	27.05/0.9571	28.66/0.9674	28.65/0.9670	28.63/0.9672	28.73/0.9678
Pelican	24.36/0.8167	23.16/0.8000	24.88/0.8438	24.79/0.8420	25.03/0.8399	25.07/0.8405
Average	23.63/0.8020	23.36/0.8055	24.71/0.8448	24.68/0.8426	24.98/0.8489	25.07/0.8506

Table 5: PSNR (dB) and SSIM values of different restoration models for MB(20,60)/ $\sigma = 15$. The best results are highlighted in **bold** and the second-best results are underlined.



Fig. 6: Deblurring performance on “Img26” with visual quality and numerical results (PSNR/SSIM). (a) Ground truth; (b) Degraded image with average kernel (9,9) and Gaussian noise level $\sigma = 15$; Restored image by (c) SV-TV [58]; (d) IDD-BM3D [9]; (e) IRCNN [59]; (f) MSWNNM [61]; (g) QWNNM* [37]; (h) QWSNM (Ours).

4.3 Analysis of Power p

In this part, the effects of power p in the weighted Schatten p -norm are studied. Table 6 reports the PSNR and SSIM values for deblurring with the power p ranging from 0.15 to 1 in the Set12 dataset. From the Table 6, it can be observed that the recovery performance of our method is relatively sensitive to the parameter p . When p is 0.95, the PSNR and SSIM of QWSNM on all

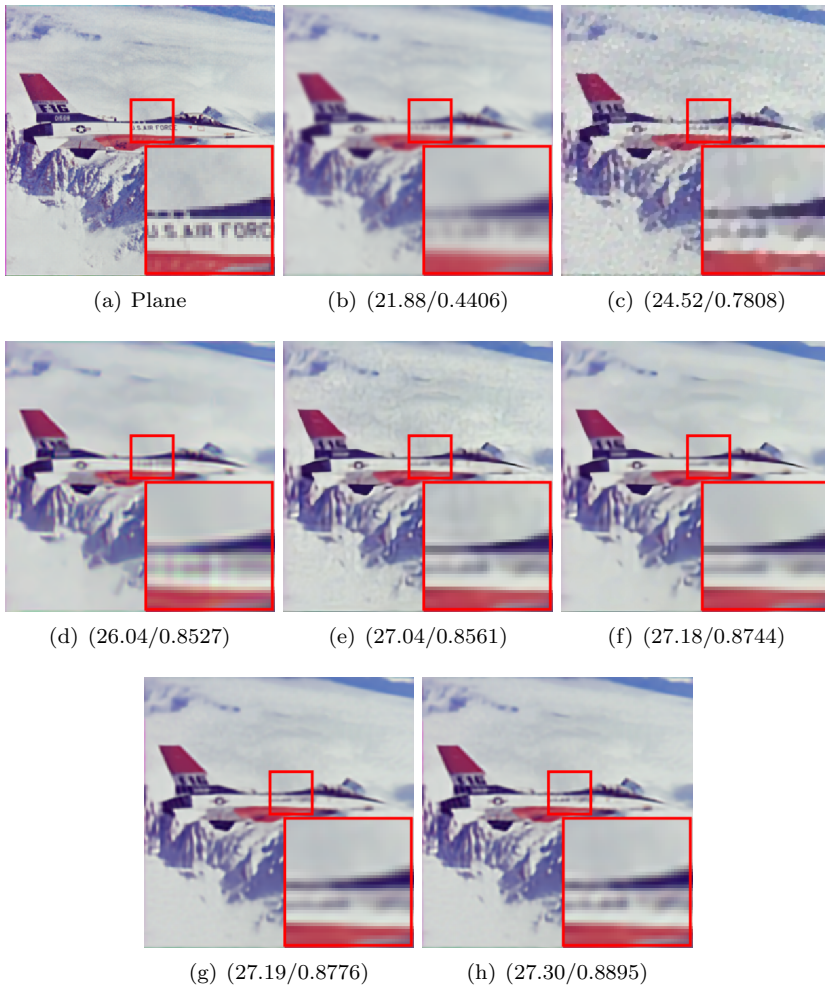


Fig. 7: Deblurring performance on “Plane” with visual quality and numerical results (PSNR/SSIM). (a) Ground truth; (b) Degraded image with Gaussian kernel (25,1.6) and Gaussian noise level $\sigma = 15$; Restored image by (c) SV-TV [58]; (d) IDD-BM3D [9]; (e) IRCNN [59]; (f) MSWNNM [61]; (g) QWNNM* [37]; (h) QWSNM (Ours).

test images consistently achieve the highest values. Therefore, p value of 0.95 is a reasonable choice for color image deblurring. To illustrate the influence of p values under different noise levels for color image denoising, we just utilize the test image “Bird” as an example and the results are presented in Fig. 9. In each subfigure, the vertical coordinate represents the PSNR value under

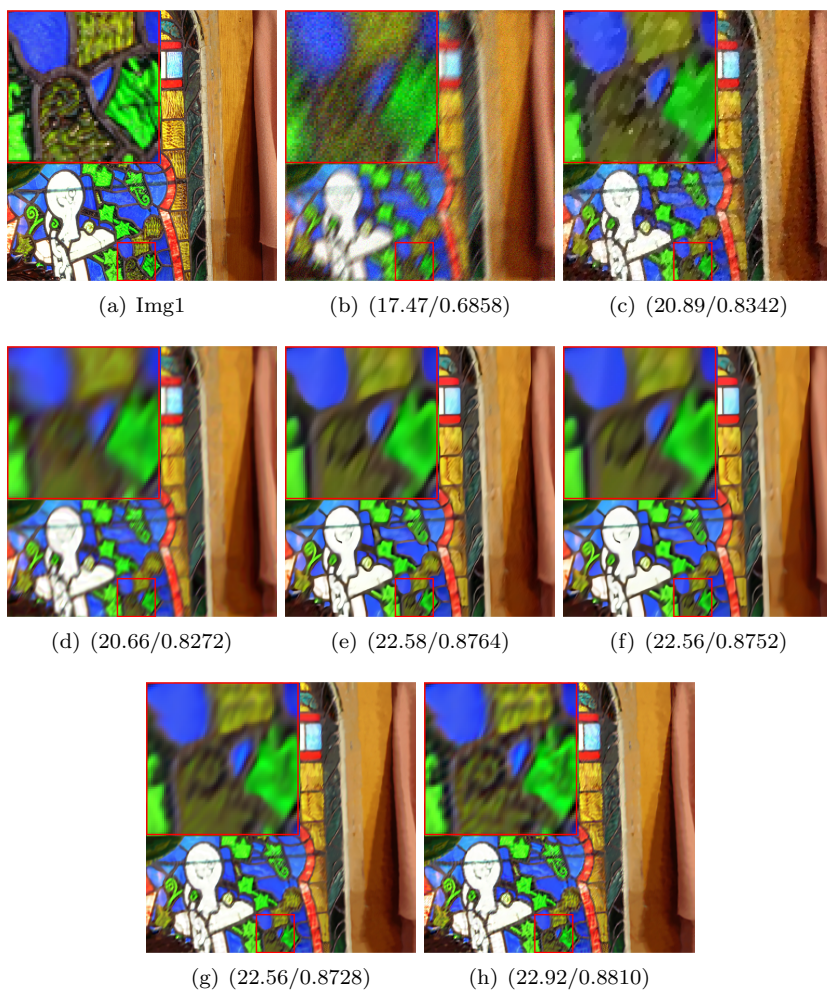


Fig. 8: Deblurring performance on “Img1” with visual quality and numerical results (PSNR/SSIM). (a) Ground truth; (b) Degraded image with motion kernel (20,60) and Gaussian noise level $\sigma = 15$; Restored image by (c) SV-TV [58]; (d) IDD-BM3D [9]; (e) IRCNN [59]; (f) MSWNNM [61]; (g) QWNNM* [37]; (h) QWSNM (Ours).

a certain noise level, while the horizontal coordinate denotes the values of p ranging from 0.1 to 1 with interval 0.05. It can be seen that when p is 0.95, our algorithm consistently achieve the highest PSNR values under different noise levels. Therefore, we also select $p = 0.95$ for color image denoising.

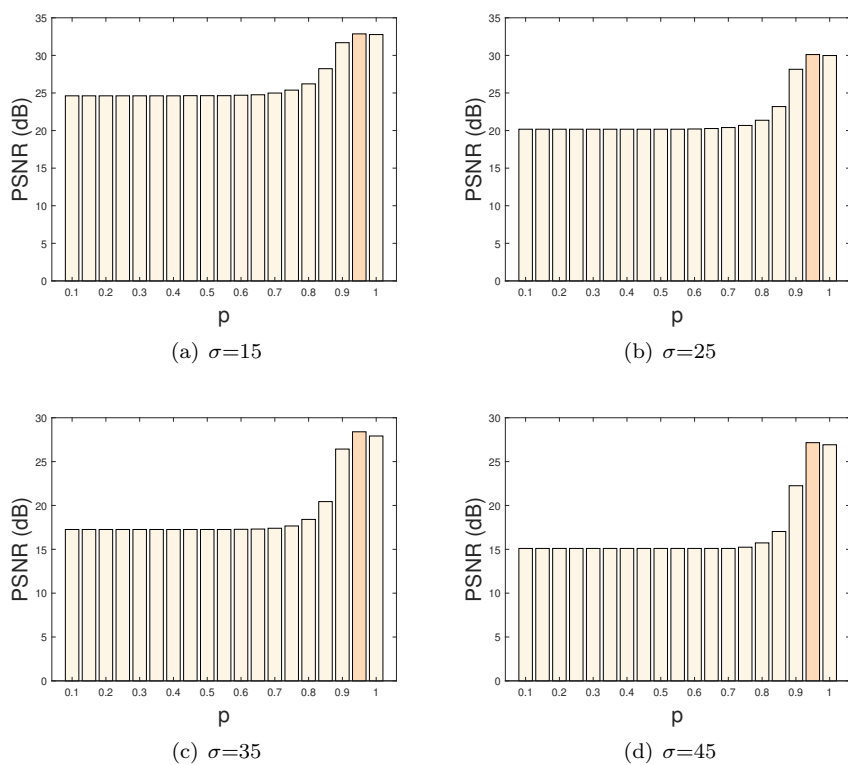


Fig. 9: The influence of changing p values on denoised results under different noise levels σ . Test image: “Bird”.

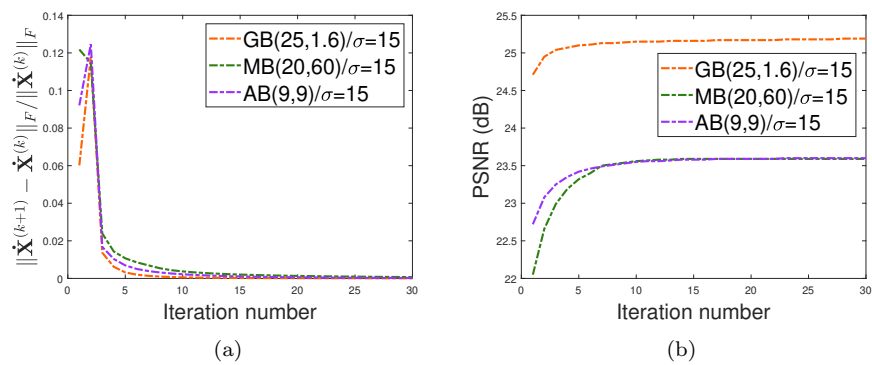


Fig. 10: The evolution curves of (a) relative error and (b) PSNR value between consecutive iterations in the case of deblurring. Test image: “Bird”.

p value	p = 0.15	p = 0.25	p = 0.35	p = 0.45	p = 0.55	p = 0.65	p = 0.75	p = 0.85	p = 0.95	p = 1
MB(20.60)/ $\sigma = 15$										
Bird	19.28/0.4117	19.28/0.4117	19.28/0.4117	19.28/0.4117	19.28/0.4117	19.33/0.4144	19.51/0.4272	20.26/0.4818	23.62/0.7425	23.41/0.7270
Plane	19.36/0.3255	19.36/0.3255	19.36/0.3255	19.36/0.3255	19.36/0.3255	19.40/0.3278	19.59/0.3389	20.37/0.3913	24.83/0.8212	24.63/0.8125
Baboon	19.06/0.5565	19.06/0.556	19.06/0.556	19.06/0.556	19.06/0.556	19.09/0.5582	19.26/0.5663	19.92/0.5977	22.30/0.7018	22.21/0.6928
Bee	20.39/0.6448	20.39/0.6448	20.39/0.6448	20.39/0.6448	20.39/0.6448	20.44/0.6469	20.70/0.6567	21.75/0.6985	28.75/0.9140	28.47/0.9117
Aquatic	18.59/0.3513	18.59/0.3513	18.59/0.3513	18.59/0.3513	18.59/0.3513	18.62/0.3535	18.78/0.3639	19.39/0.4101	24.25/0.7835	23.86/0.7690
Barbara	19.16/0.5531	19.16/0.5531	19.16/0.5531	19.16/0.5531	19.16/0.5531	19.20/0.5555	19.38/0.5664	20.07/0.6108	23.74/0.8199	23.65/0.8164
Boat	18.32/0.4238	18.32/0.4238	18.32/0.4238	18.32/0.4238	18.32/0.4238	18.35/0.4262	18.50/0.4375	19.07/0.4874	23.03/0.8072	22.50/0.7895
House	19.65/0.6424	19.65/0.6424	19.65/0.6424	19.65/0.6424	19.65/0.6424	19.69/0.6452	19.91/0.6584	20.77/0.7109	28.00/0.9300	27.19/0.9215
Peppers	19.24/0.8107	19.24/0.8107	19.24/0.8107	19.24/0.8107	19.24/0.8107	19.28/0.8123	19.46/0.8194	20.17/0.8463	24.61/0.9412	24.56/0.9415
Starfish	19.81/0.7516	19.81/0.7516	19.81/0.7516	19.81/0.7516	19.81/0.7516	18.94/0.7536	19.11/0.7622	19.77/0.7965	23.95/0.9381	23.71/0.9363
Lena	20.94/0.8271	20.94/0.8271	20.94/0.8271	20.94/0.8271	20.94/0.8271	21.00/0.8292	21.29/0.8386	22.52/0.8745	28.73/0.9678	28.63/0.9671
Pelican	19.56/0.4135	19.56/0.4135	19.56/0.4135	19.56/0.4135	19.56/0.4135	19.60/0.4161	19.80/0.4256	20.65/0.4839	25.07/0.8405	24.75/0.8332
AB(9.9)/ $\sigma = 15$										
Bird	20.33/0.4712	20.33/0.4712	20.33/0.4712	20.33/0.4712	20.34/0.4717	20.39/0.4756	20.65/0.4946	21.74/0.5868	23.55/0.7361	23.41/0.7247
Plane	20.69/0.3765	20.69/0.3765	20.69/0.3765	20.69/0.3765	20.70/0.3770	20.76/0.3808	21.04/0.3997	22.36/0.5058	25.22/0.8295	25.07/0.8224
Baboon	19.90/0.5806	19.90/0.5806	19.90/0.5806	19.90/0.5806	19.91/0.5809	19.95/0.5832	20.17/0.5936	21.06/0.6448	22.46/0.7023	22.36/0.6927
Bee	22.11/0.6941	22.11/0.6941	22.11/0.6941	22.11/0.6941	22.11/0.6941	22.19/0.6973	22.59/0.7116	24.24/0.7698	29.20/0.9186	29.20/0.9126
Aquatic	19.97/0.4135	19.97/0.4135	19.97/0.4135	19.97/0.4135	19.99/0.4142	20.04/0.4178	20.27/0.4350	21.45/0.5222	24.28/0.7874	24.15/0.7849
Barbara	20.08/0.5912	20.08/0.5912	20.08/0.5912	20.08/0.5912	20.09/0.5914	20.14/0.5945	20.37/0.6092	21.40/0.6745	23.79/0.8087	23.53/0.8053
Boat	19.55/0.4805	19.55/0.4805	19.55/0.4805	19.55/0.4805	19.56/0.4817	19.61/0.4852	19.82/0.5027	20.94/0.5942	23.17/0.8042	22.92/0.7976
House	21.51/0.7215	21.51/0.7215	21.51/0.7215	21.51/0.7215	21.52/0.7230	21.60/0.7267	21.95/0.7437	23.58/0.8137	28.95/0.9395	28.74/0.9369
Peppers	20.48/0.8458	20.48/0.8458	20.48/0.8458	20.48/0.8458	20.49/0.8467	20.55/0.8486	20.80/0.8569	21.96/0.8893	24.80/0.9440	24.72/0.9433
Starfish	20.35/0.7915	20.35/0.7915	20.35/0.7915	20.35/0.7915	20.36/0.7930	20.41/0.7954	21.66/0.8066	22.76/0.8485	24.15/0.9367	24.06/0.9373
Lena	22.19/0.9601	22.19/0.9601	22.19/0.9601	22.19/0.9601	22.20/0.9604	22.29/0.9628	22.70/0.9738	24.30/0.9104	28.60/0.9654	28.49/0.9646
Pelican	20.85/0.4638	20.85/0.4638	20.85/0.4638	20.85/0.4638	20.85/0.4638	20.91/0.4683	21.21/0.4874	22.44/0.5740	25.04/0.8362	24.95/0.8215
GB(25.1.6)/ $\sigma = 15$										
Bird	21.14/0.5421	21.14/0.5421	21.14/0.5421	21.14/0.5421	21.14/0.5421	21.21/0.5460	21.88/0.4406	23.05/0.6712	25.27/0.8130	24.98/0.7967
Plane	21.62/0.4285	21.62/0.4285	21.62/0.4285	21.62/0.4285	21.62/0.4285	21.69/0.4320	22.04/0.4494	23.89/0.5663	27.30/0.8895	26.86/0.8692
Baboon	20.54/0.6377	20.54/0.6377	20.54/0.6377	20.54/0.6377	20.54/0.6377	20.59/0.6400	20.84/0.6508	22.02/0.7096	23.48/0.7572	23.23/0.7376
Bee	22.45/0.7063	22.45/0.7063	22.45/0.7063	22.45/0.7063	22.45/0.7063	22.54/0.7090	22.97/0.7224	25.26/0.7944	31.27/0.9386	31.17/0.9375
Aquatic	21.34/0.4930	21.34/0.4930	21.34/0.4930	21.34/0.4930	21.34/0.4930	21.40/0.4965	21.71/0.5139	23.36/0.6185	26.58/0.8702	26.32/0.8597
Barbara	20.92/0.6405	20.92/0.6405	20.92/0.6405	20.92/0.6405	20.92/0.6405	20.97/0.6435	21.25/0.6581	22.61/0.7336	25.00/0.8585	24.81/0.8476
Boat	20.60/0.5385	20.60/0.5385	20.60/0.5385	20.60/0.5385	20.60/0.5385	20.66/0.5419	20.92/0.5584	22.32/0.6579	24.62/0.8524	24.20/0.8401
House	22.01/0.7448	22.01/0.7448	22.01/0.7448	22.01/0.7448	22.01/0.7448	22.08/0.7483	22.47/0.7649	24.54/0.8443	29.90/0.9500	29.61/0.9475
Peppers	21.49/0.8720	21.49/0.8720	21.49/0.8720	21.49/0.8720	21.49/0.8720	21.55/0.8738	21.88/0.8820	23.51/0.9179	26.63/0.9643	26.40/0.9604
Starfish	21.49/0.8123	21.49/0.8123	21.49/0.8123	21.49/0.8123	21.49/0.8123	21.55/0.8144	21.87/0.8250	23.53/0.8763	26.77/0.9654	26.46/0.9581
Lena	22.46/0.8675	22.46/0.8675	22.46/0.8675	22.46/0.8675	22.46/0.8675	22.52/0.8683	22.95/0.8789	25.21/0.9247	30.55/0.9800	30.27/0.9750
Pelican	21.29/0.4810	21.29/0.4810	21.29/0.4810	21.29/0.4810	21.29/0.4810	21.35/0.4820	21.68/0.4994	23.36/0.6044	26.26/0.8701	26.05/0.8615

Table 6: PSNR (dB) and SSIM values of different p values for color image deblurring on the Set12 dataset. The best results are marked in **bold**.

4.4 Convergence Study

Fig. 10 illustrates the empirical convergence of our proposed algorithm in the cases of three blur kernels on the test image “Bird”. One can clearly observe that with the growth of iteration number, all the relative error and PSNR curves decrease and increase monotonically and ultimately become flat and stable, numerically exhibiting the reliable convergence behavior of proposed QWSNM algorithm. It is noted that other scenarios also have the similar conclusions.

5 Conclusion

In this paper, we proposed a quaternion-based QWSNM model for color image restoration, which combines the advantages of the WSNM regularizer and quaternion representation. To be concrete, the WSNM regularizer can better adaptively shrink the rank components over the WNNM counterpart, and the quaternion representation of color images is capable of fully preserving the correlation of three color channels. In particular, we modified the QADMM algorithm through a continuation strategy to iteratively solve the resulting optimization problem. Moreover, rigorous convergence analysis was provided to verify the sound properties of our proposed algorithm. Experimental results on color image denoising under different noise levels and color image deblurring under three types of blur kernels demonstrated the effectiveness and robustness of QWSNM. Compared with the related competing methods, the visual results showed that our proposed QWSNM is capable of better preserving the color structure and avoiding color distortion.

However, despite the good recovery performance, our proposed algorithm has the efficiency limitation. In fact, the QSVD in the optimization process is quite time-consuming, so how to improve the algorithmic efficiency remains a significant issue. Very recently, Gai et al. [62] introduced the theory of reduced biquaternion sparse representation, which benefited from the commutative of the reduced biquaternion algebra. In the future research, we would pay more attention to the reduced biquaternion representation and extend existing algorithms to the reduced biquaternion domain for color image restoration. In parallel, we plan to extend the proposed QWNNM algorithm to other relevant tasks, such as color image inpainting, color image super-resolution and compressive sensing, etc.

Acknowledgements

The research was supported by the NSFC under Grants 12001005, 12271083.

Conflict of Interest

The authors declare that they have no known competing financial interests or personal relationships that could have appeared to influence the work reported in this paper.

Code Availability

Code generated or used during the study are available from the corresponding author on reasonable request.

References

1. Rudin, L.I., Osher, S., Fatemi, E.: Nonlinear total variation based noise removal algorithms. *Physica D: Nonlinear Phenomena* **60**(1-4), 259–268 (1992)
2. Wang, Y., Yang, J., Yin, W., Zhang, Y.: A new alternating minimization algorithm for total variation image reconstruction. *SIAM Journal on Imaging Sciences* **1**(3), 248–272 (2008)
3. Bredies, K., Kunisch, K., Pock, T.: Total generalized variation. *SIAM Journal on Imaging Sciences* **3**(3), 492–526 (2010)
4. Chang, H., Zhang, X., Tai, X.C., Yang, D.: Domain decomposition methods for nonlocal total variation image restoration. *Journal of Scientific Computing* **60**, 79–100 (2014)
5. Mairal, J., Elad, M., Sapiro, G.: Sparse representation for color image restoration. *IEEE Transactions on Image Processing* **17**(1), 53–69 (2007)
6. Zhang, J., Zhao, D., Gao, W.: Group-based sparse representation for image restoration. *IEEE Transactions on Image Processing* **23**(8), 3336–3351 (2014)
7. Zha, Z., Yuan, X., Wen, B., Zhang, J., Zhu, C.: Nonconvex structural sparsity residual constraint for image restoration. *IEEE Transactions on Cybernetics* **52**(11), 12440–12453 (2021)
8. Buades, A., Coll, B., Morel, J.M.: A non-local algorithm for image denoising. In: *Proceedings of the IEEE Conference on Computer Vision and Pattern Recognition (CVPR)*, pp. 60–65 (2005)

9. Danielyan, A., Katkovnik, V., Egiazarian, K.: BM3D frames and variational image deblurring. *IEEE Transactions on Image Processing* **21**(4), 1715–1728 (2011)
10. Peng, Y., Suo, J., Dai, Q., Xu, W.: Reweighted low-rank matrix recovery and its application in image restoration. *IEEE Transactions on Cybernetics* **44**(12), 2418–2430 (2014)
11. Dong, W., Shi, G., Li, X.: Nonlocal image restoration with bilateral variance estimation: a low-rank approach. *IEEE Transactions on Image Processing* **22**(2), 700–711 (2012)
12. Lai, R., Li, J.: Manifold based low-rank regularization for image restoration and semi-supervised learning. *Journal of Scientific Computing* **74**, 1241–1263 (2018)
13. Zhang, K., Li, Y., Zuo, W., Zhang, L., Van Gool, L., Timofte, R.: Plug-and-play image restoration with deep denoiser prior. *IEEE Transactions on Pattern Analysis and Machine Intelligence* **44**(10), 6360–6376 (2021)
14. He, L., Zhang, Q., Yang, X., Wang, Y., Wang, C.: SLN-RED: Regularization by simultaneous local and nonlocal denoising for image restoration. *IEEE Signal Processing Letters* **30**, 578–582 (2023)
15. He, W., Zhang, H., Zhang, L., Shen, H.: Total-variation-regularized low-rank matrix factorization for hyperspectral image restoration. *IEEE Transactions on Geoscience and Remote Sensing* **54**(1), 178–188 (2015)
16. Chi, Y., Lu, Y.M., Chen, Y.: Nonconvex optimization meets low-rank matrix factorization: An overview. *IEEE Transactions on Signal Processing* **67**(20), 5239–5269 (2019)
17. Shi, C., Huang, Z., Wan, L., Xiong, T.: Low-rank tensor completion based on log-det rank approximation and matrix factorization. *Journal of Scientific Computing* **80**(3), 1888–1912 (2019)
18. Ke, Y., Ma, C., Jia, Z., Xie, Y., Liao, R.: Quasi non-negative quaternion matrix factorization with application to color face recognition. *Journal of Scientific Computing* **95**(2), 38 (2023)
19. Candès, E.J., Li, X., Ma, Y., Wright, J.: Robust principal component analysis? *Journal of the ACM* **58**(3), 1–37 (2011)
20. Jin, Z.F., Wan, Z., Jiao, Y., Lu, X.: An alternating direction method with continuation for nonconvex low rank minimization. *Journal of Scientific Computing* **66**, 849–869 (2016)

21. Yuan, W., Liu, H., Liang, L., Xie, G., Zhang, Y., Liu, D.: Rank minimization via adaptive hybrid norm for image restoration. *Signal Processing* **206**, 108926 (2023)
22. Candes, E., Recht, B.: Exact matrix completion via convex optimization. *Communications of the ACM* **55**(6), 111–119 (2012)
23. Gu, S., Zhang, L., Zuo, W., Feng, X.: Weighted nuclear norm minimization with application to image denoising. In: *Proceedings of the IEEE Conference on Computer Vision and Pattern Recognition (CVPR)*, pp. 2862–2869 (2014)
24. Gu, S., Xie, Q., Meng, D., Zuo, W., Feng, X., Zhang, L.: Weighted nuclear norm minimization and its applications to low level vision. *International Journal of Computer Vision* **121**(2), 183–208 (2017)
25. Nie, F., Huang, H., Ding, C.: Low-rank matrix recovery via efficient Schatten p -norm minimization. In: *Proceedings of the AAAI Conference on Artificial Intelligence*, vol. 26, pp. 655–661 (2012)
26. Xie, Y., Gu, S., Liu, Y., Zuo, W., Zhang, W., Zhang, L.: Weighted Schatten p -norm minimization for image denoising and background subtraction. *IEEE Transactions on Image Processing* **25**(10), 4842–4857 (2016)
27. Zha, Z., Zhang, X., Wu, Y., Wang, Q., Liu, X., Tang, L., Yuan, X.: Non-convex weighted l_p nuclear norm based ADMM framework for image restoration. *Neurocomputing* **311**, 209–224 (2018)
28. Luisier, F., Blu, T.: SURE-LET multichannel image denoising: Interscale orthonormal wavelet thresholding. *IEEE Transactions on Image Processing* **17**(4), 482–492 (2008)
29. Dabov, K., Foi, A., Katkovnik, V., Egiazarian, K.: Image denoising by sparse 3-D transform-domain collaborative filtering. *IEEE Transactions on Image Processing* **16**(8), 2080–2095 (2007)
30. Xu, J., Zhang, L., Zhang, D., Feng, X.: Multi-channel weighted nuclear norm minimization for real color image denoising. In: *Proceedings of the IEEE International Conference on Computer Vision (ICCV)*, pp. 1096–1104 (2017)
31. Huang, X., Du, B., Liu, W.: Multichannel color image denoising via weighted Schatten p -norm minimization. In: *Proceedings of the Twenty-Ninth International Joint Conferences on Artificial Intelligence (IJCAI)*, pp. 637–644 (2021)

32. Chen, Y., Xiao, X., Zhou, Y.: Low-rank quaternion approximation for color image processing. *IEEE Transactions on Image Processing* **29**, 1426–1439 (2019)
33. Liu, X., Chen, Y., Peng, Z., Wu, J., Wang, Z.: Infrared image super-resolution reconstruction based on quaternion fractional order total variation with l_p quasinorm. *Applied Sciences* **8**(10), 1864 (2018)
34. Miao, J., Kou, K.I.: Color image recovery using low-rank quaternion matrix completion algorithm. *IEEE Transactions on Image Processing* **31**, 190–201 (2021)
35. Zou, C., Kou, K.I., Wang, Y.: Quaternion collaborative and sparse representation with application to color face recognition. *IEEE Transactions on Image Processing* **25**(7), 3287–3302 (2016)
36. Yu, Y., Zhang, Y., Yuan, S.: Quaternion-based weighted nuclear norm minimization for color image denoising. *Neurocomputing* **332**, 283–297 (2019)
37. Huang, C., Li, Z., Liu, Y., Wu, T., Zeng, T.: Quaternion-based weighted nuclear norm minimization for color image restoration. *Pattern Recognition* **128**, 108665 (2022)
38. Huang, C., Li, J., Gao, G.: Review of quaternion-based color image processing methods. *Mathematics* **11**(9), 2056 (2023)
39. Flamant, J., Miron, S., Brie, D.: A general framework for constrained convex quaternion optimization. *IEEE Transactions on Signal Processing* **70**, 254–267 (2021)
40. Jia, Z., Ng, M.K.: Structure preserving quaternion generalized minimal residual method. *SIAM Journal on Matrix Analysis and Applications* **42**(2), 616–634 (2021)
41. Zhang, F.: Quaternions and matrices of quaternions. *Linear Algebra and its Applications* **251**, 21–57 (1997)
42. Mei, J.J., Dong, Y., Huang, T.Z., Yin, W.: Cauchy noise removal by non-convex ADMM with convergence guarantees. *Journal of Scientific Computing* **74**, 743–766 (2018)
43. He, L., Wang, Y., Gao, S.: A support-denoiser-driven framework for single image restoration. *Journal of Computational and Applied Mathematics* **393**, 113495 (2021)

44. Hou, R., Li, F., Zhang, G.: Truncated residual based plug-and-play ADMM algorithm for MRI reconstruction. *IEEE Transactions on Computational Imaging* **8**, 96–108 (2022)
45. Tao, M., Zhang, X.P.: Study on L_1 over L_2 minimization for nonnegative signal recovery. *Journal of Scientific Computing* **95**(3), 94 (2023)
46. Wu, Z.C., Huang, T.Z., Deng, L.J., Vivone, G.: A framelet sparse reconstruction method for pansharpening with guaranteed convergence. *Inverse Problems and Imaging* pp. 0–0 (2023)
47. Wu, Z.C., Huang, T.Z., Deng, L.J., Huang, J., Chanussot, J., Vivone, G.: LRTCFFPan: Low-rank tensor completion based framework for pansharpening. *IEEE Transactions on Image Processing* **32**, 1640–1655 (2023)
48. Boyd, S., Parikh, N., Chu, E., Peleato, B., Eckstein, J., et al.: Distributed optimization and statistical learning via the alternating direction method of multipliers. *Foundations and Trends® in Machine learning* **3**(1), 1–122 (2011)
49. Sangwine, S.J.: Fourier transforms of colour images using quaternion or hypercomplex, numbers. *Electronics Letters* **32**(21), 1979–1980 (1996)
50. Liu, L., Huang, W., Chen, D.R.: Exact minimum rank approximation via Schatten p -norm minimization. *Journal of Computational and Applied Mathematics* **267**, 218–227 (2014)
51. Feng, L., Zhu, J.: Image recovery via truncated weighted Schatten- p norm regularization. In: *International Conference on Cloud Computing and Security (ICCCS)*, pp. 563–574 (2018)
52. Xie, Y., Qu, Y., Tao, D., Wu, W., Yuan, Q., Zhang, W.: Hyperspectral image restoration via iteratively regularized weighted Schatten p -norm minimization. *IEEE Transactions on Geoscience and Remote Sensing* **54**(8), 4642–4659 (2016)
53. Zuo, W., Meng, D., Zhang, L., Feng, X., Zhang, D.: A generalized iterated shrinkage algorithm for non-convex sparse coding. In: *Proceedings of the IEEE International Conference on Computer Vision (ICCV)*, pp. 217–224 (2013)
54. Xu, D., Mandic, D.P.: The theory of quaternion matrix derivatives. *IEEE Transactions on Signal Processing* **63**(6), 1543–1556 (2015)
55. Mirsky, L.: A trace inequality of john von neumann. *Monatshefte Für Mathematik* **79**(4), 303–306 (1975)

56. Wang, Z., Bovik, A.C., Sheikh, H.R., Simoncelli, E.P.: Image quality assessment: from error visibility to structural similarity. *IEEE Transactions on Image Processing* **13**(4), 600–612 (2004)
57. Wang, F., Huang, H., Liu, J.: Variational-based mixed noise removal with CNN deep learning regularization. *IEEE Transactions on Image Processing* **29**, 1246–1258 (2019)
58. Jia, Z., Ng, M.K., Wang, W.: Color image restoration by saturation-value total variation. *SIAM Journal on Imaging Sciences* **12**(2), 972–1000 (2019)
59. Zhang, K., Zuo, W., Gu, S., Zhang, L.: Learning deep CNN denoiser prior for image restoration. In: *Proceedings of the IEEE Conference on Computer Vision and Pattern Recognition (CVPR)*, pp. 3929–3938 (2017)
60. Wu, T., Huang, C., Jin, Z., Jia, Z., Ng, M.K.: Total variation based pure quaternion dictionary learning method for color image denoising. *International Journal of Numerical Analysis & Modeling* **19**(5) (2022)
61. Yair, N., Michaeli, T.: Multi-scale weighted nuclear norm image restoration. In: *Proceedings of the IEEE Conference on Computer Vision and Pattern Recognition (CVPR)*, pp. 3165–3174 (2018)
62. Gai, S.: Theory of reduced biquaternion sparse representation and its applications. *Expert Systems with Applications* **213**, 119–245 (2023)